

## INFORMATION TO USERS

This manuscript has been reproduced from the microfilm master. UMI films the text directly from the original or copy submitted. Thus, some thesis and dissertation copies are in typewriter face, while others may be from any type of computer printer.

The quality of this reproduction is dependent upon the quality of the copy submitted. Broken or indistinct print, colored or poor quality illustrations and photographs, print bleedthrough, substandard margins, and improper alignment can adversely affect reproduction.

In the unlikely event that the author did not send UMI a complete manuscript and there are missing pages, these will be noted. Also, if unauthorized copyright material had to be removed, a note will indicate the deletion.

Oversize materials (e.g., maps, drawings, charts) are reproduced by sectioning the original, beginning at the upper left-hand corner and continuing from left to right in equal sections with small overlaps.

ProQuest Information and Learning  
300 North Zeeb Road, Ann Arbor, MI 48106-1346 USA  
800-521-0600

UMI<sup>®</sup>



**University of Alberta**

**Spontaneous Motion of Liquid Drops via Self-Assembled Surface  
Modification**

by

**Gary Chia-Hao Mo** ©

A thesis submitted to the Faculty of Graduate Studies and Research in partial  
fulfillment of the requirements for the degree of **Master of Science**.

**Department of Mechanical Engineering**

**Edmonton, Alberta**

**Spring 2005**



Library and  
Archives Canada

Bibliothèque et  
Archives Canada

Published Heritage  
Branch

Direction du  
Patrimoine de l'édition

395 Wellington Street  
Ottawa ON K1A 0N4  
Canada

395, rue Wellington  
Ottawa ON K1A 0N4  
Canada

*Your file* *Votre référence*

*ISBN:*

*Our file* *Notre référence*

*ISBN:*

#### NOTICE:

The author has granted a non-exclusive license allowing Library and Archives Canada to reproduce, publish, archive, preserve, conserve, communicate to the public by telecommunication or on the Internet, loan, distribute and sell theses worldwide, for commercial or non-commercial purposes, in microform, paper, electronic and/or any other formats.

The author retains copyright ownership and moral rights in this thesis. Neither the thesis nor substantial extracts from it may be printed or otherwise reproduced without the author's permission.

#### AVIS:

L'auteur a accordé une licence non exclusive permettant à la Bibliothèque et Archives Canada de reproduire, publier, archiver, sauvegarder, conserver, transmettre au public par télécommunication ou par l'Internet, prêter, distribuer et vendre des thèses partout dans le monde, à des fins commerciales ou autres, sur support microforme, papier, électronique et/ou autres formats.

L'auteur conserve la propriété du droit d'auteur et des droits moraux qui protègent cette thèse. Ni la thèse ni des extraits substantiels de celle-ci ne doivent être imprimés ou autrement reproduits sans son autorisation.

---

In compliance with the Canadian Privacy Act some supporting forms may have been removed from this thesis.

Conformément à la loi canadienne sur la protection de la vie privée, quelques formulaires secondaires ont été enlevés de cette thèse.

While these forms may be included in the document page count, their removal does not represent any loss of content from the thesis.

Bien que ces formulaires aient inclus dans la pagination, il n'y aura aucun contenu manquant.

  
**Canada**

I was once told, "God already knows the truth!";  
and replied, "Agreed; He would welcome this version as well!"

*–Anonymous*

"On resiste a l'invasion des armees; on ne resiste pas a l'invasion des  
idees. [You can make a stand against the armies of the worlds; but  
you cannot resist an idea whose time has come.]"

*–Victor Hugo*

## ABSTRACT

The reactive-wetting phenomenon is investigated in this work. The nature of the wetting of liquid on solid surface of heterogeneous chemistry is postulated and later qualitatively proven. Through such understanding, a novel microfluidic device based on reactive-wetting has been proposed and studied. The device has been designed to enable divisions of minute liquid drops, without momentum transport, on flat surface designs. It is shown that multiple divisions and even tearing of one drop is possible. A physical explanation is developed to reveal the collapse of liquid film due to contributions from surface tension and the size parity in the surface design. Pragmatic aspects of the device has also been investigated. Phenomenologically, experiments has linked the kinetics of adsorption to the length and velocity of drops. The regime under which the kinetics operates can be inferred from the length and velocity of a drop. Simulation of the reactive-wetting phenomenon has been implemented and well-compared to observations in the experiments.

## ACKNOWLEDGEMENTS

The many people to whom I owe a debt of gratitude do not belong on an exhaustive list: this is too small a place to express adequately my appreciation for your efforts. I must thank the Alberta Ingenuity Fund, my benefactors, for the generous financial support. My supervisor Professor Daniel Y. Kwok, whose ceaseless, fiery work-ethics and subtle pedagogy has made a devotee of a detractor. The helpful supports of the mechanical machining facility, for always a piece well-made and an advice well-given. My colleagues, who had been, are, and will inescapably be asked again to devaluate my work: Steven Chai, Yu Wen Chang, Kanwarjit Gill, Maggie Han, Kelvin Issacson, Fuzhi Lu, Scott Pang, Fuzhi Tian, CJ Ukiwe, Junfeng Zhang. **Thank You.**

There can be no final category — My parents have always been the sustenance to my sanity: I cannot but to attempt something for which you could be pleased, and I truly hope you are.

# TABLE OF CONTENTS

<b>1</b>	<b>Introduction</b>	<b>1</b>
1.1	A thermodynamic description . . . . .	2
1.2	Core Concepts . . . . .	4
1.2.1	Literature . . . . .	4
1.2.2	Contact angle . . . . .	7
1.3	Organization of the thesis . . . . .	9
<b>2</b>	<b>Overview on Self-Assembled Monolayers</b>	<b>10</b>
2.1	Brief background of self-assembly . . . . .	10
2.2	Experimental methodology . . . . .	12
2.3	Characteristic of molecular monolayers . . . . .	14
2.3.1	Physisorption and chemisorption . . . . .	14
2.3.2	Head and tail functional groups . . . . .	15
2.3.3	Growth and packing structure . . . . .	17
2.4	Stability of monolayers . . . . .	22
2.4.1	Thermal stability . . . . .	22
2.4.2	Electrical stability . . . . .	23
2.4.3	Mechanical stability . . . . .	24
2.5	DRW SAM systems . . . . .	25
2.5.1	Primary amine on carboxylic acid tail-group . . . . .	25



2.5.2	Perfluoroalkanoic acid on metal surfaces . . . . .	25
2.5.3	Trichlorosilane on glass . . . . .	26
2.6	Summary . . . . .	26
<b>3</b>	<b>Methods and Procedures</b>	<b>28</b>
3.1	Background on experimental approach . . . . .	28
3.2	Solution process . . . . .	29
3.3	Micro-Contact Printing ( $\mu$ CP) . . . . .	30
3.4	Experimental procedures and error estimation . . . . .	32
3.5	Computational Method . . . . .	34
<b>4</b>	<b>Dewetting From Hydrophobic Surfaces</b>	<b>37</b>
4.1	Experimental perspective . . . . .	37
4.2	Introduction . . . . .	38
4.3	Procedures . . . . .	41
4.3.1	Experimental and Materials . . . . .	41
4.3.2	Computer Simulation . . . . .	42
4.4	Results . . . . .	43
4.4.1	Experimental Results . . . . .	43
4.4.2	Computational Results . . . . .	48
4.5	Summary . . . . .	57
<b>5</b>	<b>Length to Velocity Relationship</b>	<b>59</b>
5.1	Empirical relations . . . . .	60
5.1.1	Force balance . . . . .	60
5.1.2	Viscous force dependence on drop length . . . . .	62
5.1.3	Adsorption reaction dependence on drop length . . . . .	64
5.2	Results and Discussion . . . . .	65

5.2.1	Methods . . . . .	65
5.2.2	Combined description of the two adsorption experiments .	66
5.3	Summary . . . . .	71
<b>6</b>	<b>Application: Self-Breakup of Drops</b>	<b>72</b>
6.1	Methodology . . . . .	73
6.2	Results and discussion . . . . .	75
6.3	Summary . . . . .	86
<b>7</b>	<b>Conclusions and Future Work</b>	<b>88</b>
7.1	Summary . . . . .	88
7.2	Future direction . . . . .	89
	<b>Bibliography</b>	<b>91</b>

## LIST OF TABLES

2.1	Previously employed solvents for preparation of solution self-assembly; adopted from [11] . . . . .	13
2.2	Summarized list of known SAM system by a) Head group and substrate pair and b) Monomer species and substrate pair. Note that these pairings are fairly general. Adopted from [11] and the references therein. . . . .	16
2.3	Functional groups in order of downward increasing polarity; adopted from Bhushan [36]. . . . .	17

## LIST OF FIGURES

1.1	Young's equation and the force balance that it is representative of. The liquid is shaded to differentiate it from the vapor. . . . .	6
1.2	Captured sequential, side-view of the dewetting of DIUF water from an abrupt change in surface hydrophobicity, indicated by the vertical solid line. Time difference between the adjacent captured images is $3.6 \times 10^{-3}$ seconds. Since the frames are exactly the same in size, the slanted solid line illustrates the constant speed (0.011 m/s) at which the dewetting proceeds. . . . .	8
2.1	Schematics of monomer and self-assembly of monomers by $F1$ -Substrate interaction a) a free-floating monomer b) the molecular structure of self-assembled monolayer . . . . .	12
2.2	Schematics of representative stages of SAM growth and other structural features a)-c) The lay-down, stand-up and densely packed stages d) three characteristic angles of an adsorbed $n$ -alkanethiol monomer e) Effect of surface roughness on SAM . . . . .	18
3.1	Flow-chart of the inverted SAM and the $\mu$ CP process performed . . . . .	31

4.1	Captured image of: a) Top-view of the front and wake of a moving liquid volume under sufficient, rectangular wetting restriction; b) Macroscopic observation of the same liquid drop from the side; note that the reflection of the profile is also visible. The line in a) represents the length of 10 mm; b) is scaled differently. . . . .	40
4.2	Schematics of the experimental setup. Note the CCD camera is aligned parallel to the substrate plane. . . . .	41
4.3	The captured images of a surface-ascending liquid drop in two proof of concept experiments. The circles in each picture highlights the location of the drops, which can be seen to move to a higher position from a previous picture. . . . .	44
4.4	Schematic and captured image of asymmetric longitudinal profile; a horizontal case is provided for comparison. . . . .	45
4.5	Experimental velocity of the surface-ascending drops. Linear least-square regression gives $v = 5.49 - 10.462 \sin \theta$ , with an $R^2$ value of 0.95 . . . . .	47
4.6	LBM simulations of statics drops with each frame separated by 100 simulation steps. The substrate plane is horizontal in both cases. a) low energy surface b) high energy surface . . . . .	50
4.7	LBM simulation of an ascending drop with each frame separated by 100 simulation steps. The incline is $10^\circ$ . Each frame of the two-dimensional view has been rotated by the incline angle to convey better understanding. A three-dimensional view is provided for comparison. . . . .	51

4.8	The hydrophobicity of the solid surface ( $XY$ plane at $Z = 1$ ) supporting a surface-ascending reactive-wetting drop; substrate plane is $10^\circ$ . . . . .	52
4.9	Climbing velocity from LBM simulations. Least square regression is also plotted ( $v = 0.0462 - 0.0441 \sin \theta$ ) with a $R^2$ value of 0.99. . . . .	53
4.10	Streamline of a surface-ascending drop via LBM simulation; this $XZ$ plane is given at $Y = 10$ and intersects with the center of the drop. . . . .	54
4.11	Slices of the mass-flow field of an ascending drop against an incline of $10^\circ$ . Part a) shows cross-sections with constant $X$ values; part b) with constant $Y$ values; and part c) with constant $Z$ values. Each slice shows only the flow normal to its plane, and the direction is indicated in color: blue represents the positive and red is the negative direction. White represents stagnant flow. Density plots similar to Fig.4.7 is provided for the purpose of position comparison. . . . .	55
4.12	Pressure in a surface-ascending liquid drop through LBM simulation, obtained through material derivative $D\rho/Dt$ . . . . .	56
5.1	Schematics of the coordinate systems used in lubrication approach.	61
5.2	Numerical result without consideration of reaction mechanism; ◦ represent data from Lee et al. [17]. . . . .	67
5.3	Overall length effect for the data from Lee et al. [17]. . . . .	68
5.4	Overall length effect for data from Santos and Ondarçuhu [57]. . .	68

5.5	Observed length and velocity response for a dodecylamine(DHN)/-thiol/gold system. . . . .	70
6.1	Captured image of: a) Top-view of the front and wake of a moving liquid volume under sufficient, rectangular wetting restriction; b) Macroscopic observation of the same liquid drop from the side; note that the reflection of the profile is also visible. The line in a) represents the length of 10 mm; b) is scaled differently. Note that the front geometry of a) is nearly symmetric about the center of the rectangular track. . . . .	74
6.2	Schematics of the branching hydrophobic surface modification and its anticipated effect . . . . .	74
6.3	Captured sequential (top-to-bottom), top-view images of: a) The splitting of a liquid drop b) Performing three divisions on a single liquid volume. The restriction geometry is given to guide the eye. The dimension lines provided represent 10 mm; the quantity beside each image represent the time elapsed in seconds. . . . .	76
6.4	Trial hydrophobic junction geometries and their respective performance . . . . .	78
6.5	Captured top-view image of: a) A hydrophilic area being covered by the liquid volume due to surface tension. b) The <i>pinching</i> effect; the satellite volumes may be located at the point of the arrow. c) The junction design; shaded region represents a hydrophilic area. The restriction geometries are provided to guide the eye. . .	78

6.6	Diagrams of the geometry employed for analysis of narrow wetting passage; the shaded area allows monolayer formation. The drop translates in the direction of the thick arrows. . . . .	79
6.7	Average response of reactive-wetting drops on narrow junctions, characterized by ratio $(R_1 - d)/L$ a) vibration-isolated b) under vibration . . . . .	82
6.8	Laplacian flow inside narrow reactive-wetting drops through LBM simulation. The figures are simulations representing different rates of surfactant adsorption, which is adjusted through Eq. (4.1). Simulations in a) were performed with the parameter $k = 0.001$ ; those in b) were performed with the parameter $k = 0.01$ . . . . .	85



# NOMENCLATURE

## LATIN SYMBOLS

- $A$  ..... Thermodynamics: two-dimensional area of an interfacial region
- AFM ..... Atomic Force Microscopy
- BGK ..... Bhatnagar, Gross, and Krook approximation to Boltzmann collision integral
- DIUF ..... De-ionized, ultra-filter
- EOH ..... Ethanol
- FTIR ..... Fourier-Transform Infrared (Spectroscopy)
- $F_v$  ..... Viscous force
- $F_\gamma$  ..... Unbalanced surface force
- $g$  ..... Gravitational constant
- ICPRIE ..... Inductively-coupled plasma reactive ion etch
- LBM ..... Lattice Boltzmann Method
- (D)RW ..... (Discrete-drop) Reactive Wetting

$S$  ..... entropy

$u$  ..... fluid velocity normal to the liquid-vapor interface

$U$  ..... internal energy

$V$  ..... Chapter 1: volume;  
Chapter 5: average velocity

$N$  ..... number of molecules of a species

SAM(s) ..... Self-Assembled Monolayer(s)

#### GREEK SYMBOLS

$\gamma_{sv}$  ..... solid-vapor surface tension

$\gamma_{sl}$  ..... solid-liquid surface tension

$\gamma_{lv}$  ..... liquid-vapor surface tension

$\theta_a$  ..... advancing contact angle

$\theta_r$  ..... receding contact angle

$\theta_Y$  ..... Young contact angle

$\psi$  ..... tilt angle for  $n$ -alkanethiol monolayers

$\phi$  ..... Chapter 2: rotational angle for  $n$ -alkanethiol monolayers;  
Chapter 5: tangent to the liquid-vapor interface;  
Chapter 6: scalar potential of the fluid velocity normal to the  
liquid-vapor interface

$v$  ..... One-dimensional velocity profile of the droplet

$\rho_a$  ..... Density (of the species **a**)

$\mu$  ..... viscosity

$\zeta$  ..... location in terms of vertical distance of the liquid-vapor interface

# CHAPTER 1

## INTRODUCTION

The surfaces of the objects of our daily routines are practically ignored because they are no more significant than aesthetics. Typically, it is the bulk that contributes to the properties in which we are interested. For example, the strength of steel is not necessarily related to its surface polish. But in many modern industries, as we work increasingly at a limit of small volume to surface ratio, our expectations based on the bulk behavior of substances are eroded by the characteristics and properties of the surface. It is for this reason that the field of interfacial science has received an exponential growth in interest and consequently a tremendous amount of research effort in the past 15 years [1]. This investigation, however, is an indirect effort to understand surface effects — through a delightfully simple experiment.

In 1963, in the Kendall Award Symposium honoring William A. Zisman, there was the report regarding an interesting phenomenon: Droplets of oils are compelled to shift toward another region on a flat surface. The droplets contained merely some surfactant chemicals and no external forces on the drops were required. This phenomenon is now known as Reactive Wetting; henceforth it will be abbreviated using **DRW** (Discrete-drop Reactive Wetting). In its most humble version, the solution of a surface-active-agent (or *surfactant*) is simply placed

on a corresponding substrate, via a syringe. The surfactants then quickly modify the contacted substrate surface, forming a mono-molecular film called Self-Assembled Monolayers (SAM). The effect of this surface modification is simple: the solution volume continuously displaces itself to another location on a substrate. The phenomenon remains fascinating even today: it is simply fantastic to see something move by itself. The droplet translates by first wetting a substrate region adjacent to its previous wetted edge. This is called the front. Having expanded its wetted area and correspondingly made thin the film height, the front continues to advance, while at a critical point the rest of the liquid volume is dragged along in what is called a wake. The perspective of the observer is that of the droplet moving, at approximately constant velocity, across the substrate until all surfactant species is effectively consumed. This thesis addresses this phenomenon through experimental and computational methods, developing an explanation for the mode of transport and a practical microfluidic device from reactive-wetting drops.

### **1.1 A thermodynamic description**

The apparent simplicity in a DRW deceives, however. The volume is not acted upon by any external forces or potential. The instantaneous direction of the liquid, as an average, seems to depend little on its momentum at a previous, arbitrarily small time. Its transient responses are beautiful yet perplexingly irregular and random. Directly, a question comes to mind: how is it that the volume displaces itself; what is the nature of the motion? Macroscopic constraints in the experiments specifies or validate that no influx of energy in the form of temperature, electrical/gravitational/magnetic potential, or pressure is present. Thus, a DRW

system is not achieved via a direct, energy transport scheme. Then, perhaps, the system is entropic. This would be intuitive with regard to the observed randomness in the motion and the spontaneity of the SAM formation. For instance, it is held that the thermodynamic derivative:

$$\gamma = \left( \frac{dU^A}{dA} \right) \Big|_{(S^A, N^A)} \quad (1.1)$$

represent trivially the energy content of an unit interfacial area.  $U^A$ ,  $A$ ,  $S^A$ , and  $N^A$  represents respectively the thermodynamic internal energy of the interfacial area, the interfacial area, the entropy, and the number of molecules of a species. The subscript  $A$  signifies the Gibbs interface. This is clearly an useful notation for a surface phenomenon such as the DRW. One would then define reactive-wetting as a surface energy gradient driven event, which is a natural extension of the definition of  $\gamma$ . Given below are some more observations one can make regarding DRW:

- A liquid drop with insufficient surfactant concentration does not translate.
- A DRW drop does not translate across its own footprint.
- A liquid drop containing the same surfactant species does not translate on the footprint of a previous DRW drop.
- A DRW drop can be elongated by holding the trailing, dewetting wake. Disturbing the wetting front causes the translation to cease.

It can be deduced from these facts that the following must be true:

$$\gamma_{sl,RW} > \gamma_{sl,S} \quad (1.2)$$

where subscript  $S$  refers to the original substrate surface which supports DRW, and  $RW$  refers to a spectrum of states possible by surfactant adsorption. The adsorption process effects a liquid movement only when the surface energy difference established is sufficiently large. The front contact line wets the region adjacent to it, in order to reduce the total free energy of the system since  $\gamma_{sl,S}$  is lower. Since temporary disturbances introduced at the wake do not inhibit the translation, the wake is merely dragged along by the front edge. Surface tension of the liquid dictates its relaxation, hence how far the liquid drop can elongate before a contractile response. A DRW cannot traverse its own footprint because the surface energy has already been modified, and to wet it represents an increase in total free energy.

## 1.2 Core Concepts

Aside from self-assembled monolayers, which is discussed in the following chapter, several fundamental concepts warrants introduction before a useful investigation into DRW can ever be made.

### 1.2.1 Literature

A brief overview of the literature which applies directly to the DRW problem will be visited. Brochard and coworkers has published fluid dynamical analyses on drops translating due to chemical or thermal gradient [2, 3]. It is customary in these approaches to begin with the hydrodynamic force balance across the contact line:  $F_Y = F_v$ . The driving force is designated  $F_Y$ , and is the unbalanced surface force due to thermal gradient within the fluid (the Marangoni effect) or chemical/wetting heterogeneity on the surface.  $F_v$  represents the viscous forces due to the motion of the drop on the surface. By enforcing a no-slip boundary

condition at the substrate and no-flow at the free surface (liquid-vapor interface), the lubrication approximation is obtained, which gives the Poiseuille flow profile  $v(z)$  in the drop as a function of an average drop velocity  $V$ :

$$v(z) = \frac{3V \cdot (2z\zeta - z^2)}{2\zeta^2} \quad (1.3)$$

where  $z$  is the vertical position, and  $\zeta$  is the height of the free surface at the given position. The viscous force can then be expressed as

$$F_v = \int \mu \frac{dv}{dz} dx, \quad (1.4)$$

where  $\mu$  is the viscosity of the liquid employed as DRW drop. For a chemical, wetting heterogeneity, the driving force is not so straight-forward. The prevailing method is an estimation employing static contact angle values. In this approach, the static contact angles of a fully surfactant-modified substrate and also a non-functionalized virgin substrate are taken carefully. Young's equation, which governs the static equilibrium of a liquid drop, is then utilized:

$$\gamma_{lv} \cos \theta_Y = \gamma_{sv} - \gamma_{sl}, \quad (1.5)$$

where  $\gamma_{lv}$ ,  $\gamma_{sv}$ ,  $\gamma_{sl}$  are the surface tension of the liquid-vapor, solid-vapor, and solid-liquid interfaces, respectively. The contact angle  $\theta_Y$  is called the Young contact angle. Young's equation can be visualized as the force balance at the three-phase contact line, see Figure 1.1. With this concept, it is obvious that the unbalanced surface force due to chemical heterogeneity can be expressed as

$$F_Y = \gamma_{lv} (\cos \theta_a - \cos \theta_r). \quad (1.6)$$



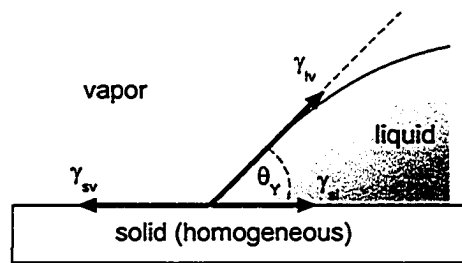


Figure 1.1: Young's equation and the force balance that it is representative of. The liquid is shaded to differentiate it from the vapor.

In this case the advancing contact angle  $\theta_a$  is smaller than the receding contact angle  $\theta_r$ . This is because the receding edge in a DRW must contact less wettable surface regions when compared to the advancing edge. Hence when the approximation is made with Young contact angles, the receding contact angle must be larger than the advancing contact angle to produce a force favorable for drop motion in the direction of the advancing edge.

Employing the above fluid dynamics and the force balance, a rolling, circulating flow develops in the drop [2, 4]. The result of a hydrodynamical analysis shows that the flow inside is the superposition of Poiseuille flow and shear flow, which introduces a plane of zero fluid velocity and a circulation within the DRW drop. A recent study has observed a similar rolling flow in a wetting/dewetting drop similar to a DRW drop utilizing atomic or molecular collision model [5].

The dynamics of the three-phase contact line and the liquid-vapor interface is a very active topic of research. Here, only a few works that are of direct interest to DRW will be noted. de Gennes predicted a precursor film which announces the motion of the three-phase contact line during complete wetting, or zero equilibrium contact angle [3]. This has been shown experimentally by many authors, for example [6, 7]. The precursor film is several hundred angstroms in thickness,

obviously invisible to the naked eye and is typically hundreds of micrometers in advance of the visible contact-line. The dynamics of the liquid-vapor interface has very recently been formulated for a specific problem through a classical velocity potential [8]. Using this method, a evolutionary simulation can be performed, resulting in an accurate description of the visible liquid-vapor interfacial position.

### 1.2.2 Contact angle

Contact angle is, individually, a very complex field of study. It is the angle that a contacting fluid apparently makes with the solid surface. Briefly, the contact angles in a DRW experiment are phenomenological quantities, effected by factors such as liquid surface tension, solid surface potential, and the wetting dynamics of the liquid bulk. Dynamic contact angle values are more complicated than conventional, static contact angles, which can be described by the thermodynamic Young equation (Eq. (1.5)) where  $\theta_Y$  is recognized to be the Young contact angle. This is an idealized value for liquid contact angle on surfaces where chemical and physical heterogeneities are absent. The use of dynamic contact angle values in a model that employs Young's equation cannot be justified thermodynamically. However, it has been shown that static contact angle can be utilized to measure solid surface energy [9], hence approximation of chemical heterogeneity.

Figure 1.2 illustrates the dewetting of a drop when in contact with an abrupt change in hydrophobicity, captured at 2500 frames per second. DIUF water is employed to emphasize the contact angle values. In this simple trial, momentum transport within the drop is minimized, and the wave-like rebound is dissipated within a very short time. It is observed that the advancing ( $\theta_a$ , front) and receding ( $\theta_r$ , back) contact angles are of similar values. This is different from the common

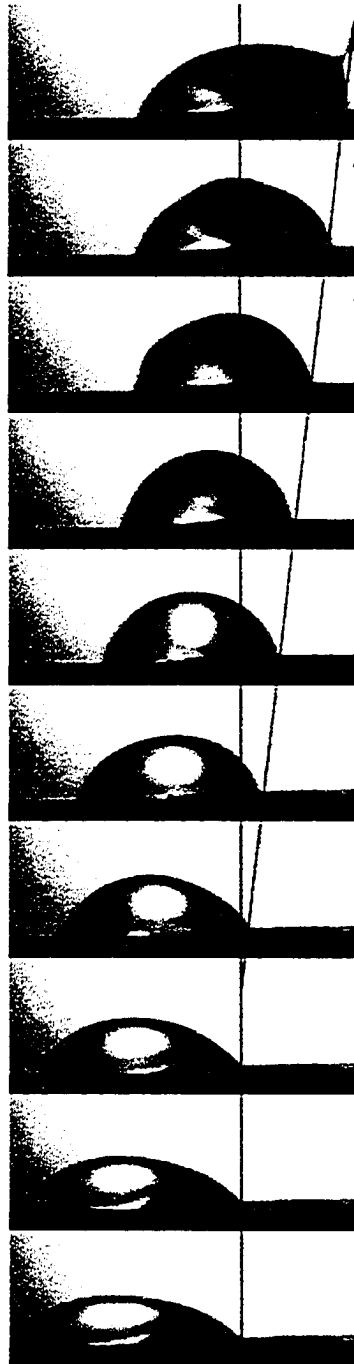


Figure 1.2: Captured sequential, side-view of the dewetting of DIUF water from an abrupt change in surface hydrophobicity, indicated by the vertical solid line. Time difference between the adjacent captured images is  $3.6 \times 10^{-3}$  seconds. Since the frames are exactly the same in size, the slanted solid line illustrates the constant speed (0.011 m/s) at which the dewetting proceeds.

notion that a contact angle reflects only the local wetting characteristic, in which case the receding (dynamic) contact angle should at all times be larger than the advancing (dynamic) contact angle. There are several simulations of this particular experiment which predict that the angles of contact corresponds to their respective local hydrophobicity (*i.e.*  $\theta_r > \theta_a$ ). This demonstrates clearly that the dynamic contact angles in DRW is phenomenological, poorly understood, and unsuitable for rigorous calculations when Young's equation is involved.

### 1.3 Organization of the thesis

Chapter 2 briefly reviews the self-assembling molecular structures that are the basis for most of the work on DRW. Although the specific details will not be relied upon heavily, the concept of self-assembled monolayers is helpful in the following discussions. The experimental procedure, error estimation, and an implementation of the computing scheme is detailed in Chapter 3. Chapter 4 begins the discussion of the reactive-wetting and introduces the combined experimental and computational approach. The application of this approach on surface-ascending discrete liquid drops is presented. The phenomenological length of a constrained liquid drop, and its effect on the velocity of the drop is investigated in Chapter 5. Chapter 6 presents a significant application of the DRW scheme in digital microfluidics. The technique enables the manipulation and transportation of discrete drops, hence the efficient use of the limited space on microfluidic chips. The thesis concludes in Chapter 7, and establishes a hypothesis to the nature of reactive-wetting using a statistical method.

## CHAPTER 2

### OVERVIEW ON SELF-ASSEMBLED MONOLAYERS

Among the many topics in interfacial science, surface functionalization has been a strong discipline for its obvious significance: the manipulation and design of surface characteristics will facilitate the engineering of matters at previously impossible small dimensions. In this context, one can begin to appreciate the ultra-thin molecular film called Self-Assembled Monolayer (SAM), and its practical applications. Due to the immense volume of literature on the subject, it is by no means possible to include all representative works on the subject and cover all possibilities of self-assembly in a few pages. The aim of this chapter is to provide a brief review of the fundamental concept of self-assembly, with particular emphasis on the straight-chain hydrocarbon mono-molecular layers employed in the DRW experiment.

#### **2.1 Brief background of self-assembly**

The history of self-assembly is not well communicated through the modern terminology. Strictly speaking, the topic is of old origins, and brief historic accounts can be found in a book by Ulman [10], and a recent comprehensive review by Schreiber [11]. Self-Assembly, for the purposes of this chapter, refers to the generic method of forming/growing molecular, aggregate structures from

surrounding environment onto a substrate through energetic and chemical means. The deposition of monolayers is indirect, since the component monomers are not kinetically inclined, such is the case for thermal evaporation, sputtering, vapor deposition, and molecular beam epitaxy. Self-Assembly also differs from conventional methods since the structure is formed through either energetic interactions or chemical bonds between a target substrate and the monomers. Self-assembly is distinct from general adhesion deposition such as spin coating and solution casting. Deposition through self-assembly is referred to as growth in the truest sense of the word: the structure expands itself with increasing monomeric count like an organism. Within this definition, methods resulting in other two-dimensional structures such as Langmuir-Blodgett (LB) technique, and reactive Chemical-Vapor-Deposition (CVD) are also considered self-assembling. Other than these thin surface coatings, self-assembly of a three-dimensional, macromolecular structure is also possible. Helical rosette nanotubes can be built out of monomers that self-assemble through hydrogen-bonding in solution [12, 13]. Nanotubes can also be formed from peptides or surfactant-like proteins [14, 15]. These examples serve to convey the potential of molecular self-assembly as a powerful approach to construct materials with novel functionality.

Within the various forms of self-assembly, research in the SAMs of long-chain hydrocarbons, with characteristic functional groups at both terminals of the backbone, proved especially productive. The structure of the monomer is advantageous in that it offers variability in a limited dimension. Figure 2.1a) illustrates a typical schematic view of such a free-floating hydrocarbon chain. The attachment of a desired functional group onto the position of either  $F1$  or  $F2$  is possible through known and well-developed chemical techniques [16]. In the presence of a solid

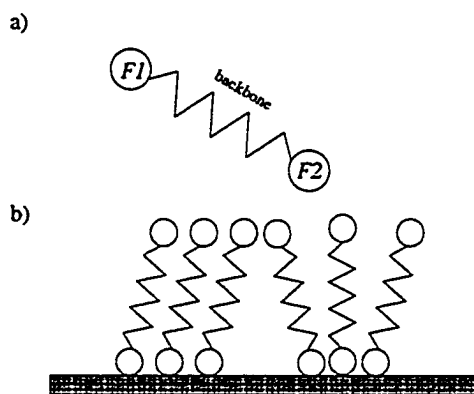


Figure 2.1: Schematics of monomer and self-assembly of monomers by  $F1$ -Substrate interaction a) a free-floating monomer b) the molecular structure of self-assembled monolayer

substrate surface, the monomers have additional configurations in which to reduce the system free energy. If the surface has preferential interaction with only functional group  $F1$  (head), the monomers then assume the thermodynamically stable configuration in Fig. 2.1b), exposing the functional group at  $F2$  (tail). The aggregate structure is of mono-molecular thickness and nearly two-dimensional. This adsorption process is the basis of SAM. It is also possible to introduce additional layers on top of this monolayer once it has been formed [17]. Throughout the chapter, examples and significant numerical values will be given for the archetypal system of alkanethiol [ $\text{CH}_3(\text{CH}_2)_n\text{SH}$ ] on gold ( $\text{Au}(111)$ ) substrate. This system has been well-studied and the representative numerical values convey a physical relevance to the otherwise qualitative discussions.

## 2.2 Experimental methodology

A medium (or mobile phase) is required for the diffusion and adsorption of monomers in the formation of a SAM. This medium is usually a liquid, an organic solvent

Solvent name	Chemical composition
ethanol	$\text{CH}_3(\text{CH}_2)\text{OH}$
decahydronaphthalene	$\text{C}_{10}\text{H}_{18}$ (aromatic)
octane	$\text{CH}_3(\text{CH}_2)_6\text{CH}_3$
cycloalkane	$\text{C}_n\text{H}_{2n}$
toluene	$\text{CHC}_6\text{H}_5$
chloroform	$\text{CHCl}_3$

Table 2.1: Previously employed solvents for preparation of solution self-assembly; adopted from [11]

with appropriate solubility for the monomer. Solubility is critical as it determines the free energy of the monomers in the liquid. Adsorption by chemisorption/physisorption is essentially a thermodynamic state change. Increased solubility is an additional thermodynamic barrier to SAM formation. As a result, ethanol and hexane are typically employed as solvents in the preparation of alkanethiol SAMs. Formation of trichlorosilane monolayers on silicon oxide, however, require water content in the solution or a hydrated surface layer for reaction purposes [18]. A sample of solvents known to be employed for solution growth of SAMs are listed in Table 2.1. The immersion time of a surface in the solution is also important. In general, higher solution concentration results in faster monolayer formation, and longer exposure time results in denser packing of the structure [19–22].

A typical experimental procedure for the preparation of an alkanethiol SAM is as follows: An ethanoic solution of monomers at millimolar (mM) concentration is prepared. The solute must be completely dissolved before use to ensure the cleanliness of the solution and the substrate. A freshly prepared substrate is immersed in the solution for 5 minutes to > 12 hrs, during which the background environment is controlled in temperature and humidity. The substrate is then re-



moved from the solution, rinsed with DIUF water and ethanol to remove excess solution, and dried using filter nitrogen. If the SAM is not required immediately, it is carefully stored in low vacuum to avoid contamination or reaction depending on the SAM chemistry. The stored sample is employed within 48 hrs.

There have been reports of SAM formation through monomers in gas phase [23]. This is very similar to typical ultra-high-vacuum (UHV) processes; in fact UHV chambers can be employed (with some alterations) to allow gas phase adsorption of SAMs. Solution processes are emphasized here since they are more prevalent in the preparation of monolayers and is exactly one of the physical processes of the DRW.

## **2.3 Characteristic of molecular monolayers**

### **2.3.1 Physisorption and chemisorption**

Adsorption of chemical species onto a substrate takes two elementary paths: electrostatic attraction or reaction forming chemical bonds. The first is often referred to as physisorption, and the latter chemisorption. Physisorption has an older history, being first reported as early as 1946 and could well have overlooked precedences. It is described that long, aliphatic, dipolar molecules can form close-packed mono-molecular thin-films spontaneously from certain non-polar solvents. Specifically Zisman observed perfluoroalkanoic acid monolayers on platinum substrates [24]. The basis for such attraction between the monomers and substrate is electrostatic. For this reason the association between the SAM and the substrate is far weaker in strength than in chemisorption, where a reaction. In the case of alkanethiols, deprotonation takes place and the H-S bond is replaced by an Au-S bond [1, 25–27]. Physisorbing monolayer will be specifically noted,

since it is the convention to call monomolecular chemisorbing films as SAMs. Physisorption has a number of advantages over chemisorption in terms of applications. Its weak nature extends to ease of cleaning and recyclable components. The removal of physisorbing films can be accomplished by a bath in a sufficiently polar fluid; de-ionized water is a typical choice [17]. The monolayer, already in a thin-film form, can further be exchanged spontaneously for a more polar species, typically a longer backbone length.

### 2.3.2 Head and tail functional groups

The head and tail functional groups on the backbone / (hydrocarbon) chain identify the SAM and determine the main characteristics of the essentially two-dimensional structure. The chemical reactivity of the head group determines the bonding (or interaction) between the substrate and the monomer species. Thus, for a given choice of substrate, the head group variation is limited. A few systems which have been reported are summarized in Table 2.2. Interaction energy between the substrate and the head group varies significantly between systems. For example, the chemical bonding formed between alkyltrichlorosilane and glass is covalent (Si-O-Si); while the popular *n*-alkanethiol-Au system has interaction strength approximately between physisorption and covalent bonding; this magnitude of interaction is typically generalized as chemisorption. The substrate-head group interaction contributes greatly to the long-term structure of the SAM.

The possibilities offered by self-assembled monolayers rest predominantly with the fact that the many facets of organic chemistry may be shifted from statistical phases (i.e. solutions, gases, etc) to two dimensional surfaces. With few restrictions (save perhaps a steric factor), the tail group is essentially a free variable

	Head group or Monomer species	Suitable substrate
a)	thiol (-HS)	Au, Ag, Cu, GaAs, Mg(I)
	selenol (-SeOH)	Au
b)	fatty acid	Ag, Al <sub>2</sub> O <sub>3</sub>
	stearate (-C <sub>17</sub> H <sub>35</sub> COOH)	calcite surfaces
	alkylamino-, alkylalkoxy-, alkyltrichloro-silane	hydroxylated surfaces (mica, oxidized-silicon, glass)
	dialkyl (di)sulfide; alkyl xanthate; dialkylthiocarbamate	Au, Ag, Cu, Pt, Mg, Fe, GaAs, InP

Table 2.2: Summarized list of known SAM system by a) Head group and substrate pair and b) Monomer species and substrate pair. Note that these pairings are fairly general. Adopted from [11] and the references therein.

where one can tailor the exposed surface chemistry; for example, the derivative an OH-terminated SAM [28–32]. Voluminous works are available describing the chemical and mechanical changes granted to surfaces via self-assembled layers bearing designed functional groups. For example, one can certainly demonstrate wettability change on a treated surface through contact angle variations [33]. In these experiments, surfaces are made relatively more hydrophilic or hydrophobic by presenting (at the SAM surface) polar or non-polar functional groups, respectively. For reference, relative polarity of some basic organic functional groups, which can be utilized to vary the exposed surface properties, are compiled in Table 2.3. The contact angle, in response to the surface treatment, decreases for more hydrophilic surfaces and vice versa. It is also possible to alter the chemical reactivity of the substrate; here the possibilities are endless due to the variability and interesting properties of organic species available to modern chemistry. As an interesting step toward future applications, ligands have recently been attached to the tail positions of an alkanethiolate monolayer (each via a linker moiety) to enable chemical interactions of the SAMs with proteins and cells [34]. This enables

Functional group	Chemical formula
methyl	-CH <sub>3</sub>
aryl	-(benzene ring)
trifluoromethyl	-CF <sub>3</sub>
trichlorosilane	-SiCl <sub>3</sub>
thiol	-HS
amide	-CONH <sub>2</sub>
amine	-NH <sub>2</sub>
carbonyl	-CO
aldehyde	-COH
carboxyl	-COOH
alcohol	-OH

Table 2.3: Functional groups in order of downward increasing polarity; adopted from Bhushan [36].

a new set of tools for research in cell biology, and supports future applications of lab-on-a-chip or micro-arrays for chemical analyses. It is also possible to form multiple monolayers similar to multiple applications of the LB technique [35]. In this case, the tail group of the already formed monolayer has affinity for the head group of another monomer, which can be grown on top of the previous layer through similar solution depositions.

### 2.3.3 Growth and packing structure

The time dependent growth of a monolayer is illustrated in Figure 2.2, in three representative stages: lay-down phase, stand-up phase, and packed monolayer. This concept of the formation of SAM has been verified by dynamic measurements on immersed substrates in many studies through the use of surface characterization techniques. Techniques such as ellipsometry (which measures the thickness of thin films through changes in optical constants  $n$  and  $k$ ) [37], Fourier Transform Infrared Spectroscopy (FT-IR, which gives the bond-specific vibrational spectra

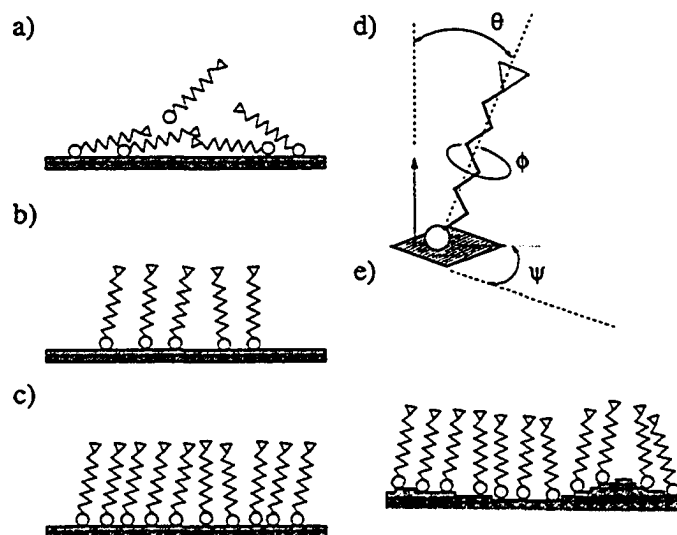


Figure 2.2: Schematics of representative stages of SAM growth and other structural features a)-c) The lay-down, stand-up and densely packed stages d) three characteristic angles of an adsorbed *n*-alkanethiol monomer e) Effect of surface roughness on SAM

of the surface species) [38], and Surface Plasmon Resonance (SPR, which measures changes in bulk solution refractive index) [39] can be employed for static as well as dynamic studies of the growth. These techniques allow one to infer the most probable SAM structure for a given chemistry of the system. Other techniques such as scanning tunneling microscopy (STM) are not particularly suitable for dynamic measurements, but provides direct observation of the SAM structure [40]. These observations serve as benchmarks in the verification of structures inferred from dynamic techniques.

In the early stage of SAM formation, the head groups adsorb onto the substrate as shown in Figure 2.2a). This is often called the lay-down phase of the formation. There is little packing at this stage, as the adsorption is often random-sequential, with very few monomers desorbing from the substrate. As more ad-

sorption takes place, the structure begins to resemble that shown in Fig. 2.2b). The monomers stand-up and self-organize, by virtue of thermodynamic equilibrium, into a packed structure. As there are still spaces available on the substrate for further head group adsorption, the final equilibrium structure closely resembles that shown in Fig. 2.2c). Eventually, the entire exposed substrate is coated with a mono-molecular layer of the monomer species. Equilibrium may be reached sooner by the diffusion of species at higher concentrations. For alkanethiol SAMs, immersion of a gold substrate in a 5 mM solution of octadecanethiol for 5 to 10 minutes forms a 90% packed SAM structure [20]. A significantly long immersion time of typically 24 hrs is required before a completely packed monolayer can be obtained. As a first approximation first-order Langmuir growth models can be employed accurately for the theoretical coverage of a SAM on its substrate. But small substrate contaminations can easily propagate and result in a significantly different evolution of coverage with respect to time [41, 42]. Other defects such as surface roughness and solution cleanliness can also amplify themselves transiently due to the reduced dimension of monolayers. Unless formation kinetics is the object of study, long substrate immersion time is preferred. However, unreasonably long immersion period might lead to other complications. Issues including the contamination from the surroundings, swelling or degrading of surfaces, evaporation of the solution, and the recrystallization of monomer species are all possible detriments.

Since the head groups in the liquid pre-cursor phase will not adsorb onto the tail group of the SAM, the growth of multiple-layers is not promoted in this solution process. Note that island nucleation has been observed during the initial stage [43] which is typical for long-backbone species; coalescence of islands oc-

curs with longer immersion time. An important feature of the final structure is a cant of attachment to the substrate often called the canted angle  $\theta$ , as shown in Fig. 2.2d). The canted angle can be attributed to a crystalline or amorphous structure of the substrate (which the head group follows), the intrinsic asymmetry of the monomers, and the steric requirement of functional groups at the tail. Studies have shown that the substrate effect dominates other factors [1]. The average value of the canted angle for a specific SAM, which can be obtained through various techniques, is qualitatively useful in determining the type of SAM structure on the substrate. The equilibrium structure of the monolayer can be experimentally observed/inferred, or theoretically predicted using molecular dynamics [44]. For octadecanethiol, the canted angle is around  $28^\circ$ , while for other systems the canted angle ranges from zero (silane systems) to  $>55^\circ$ . With a give system, one may infer from an unusually large average canted angle that the SAM is poorly formed as most of the monomers are possibly in the lay-down phase. An unusually small canted angle of a known system can be explained as the stretching/bending of the hydrocarbon backbones. Designated as  $\phi$  on Fig. 2.2d), the rotation angle refers to the twisting of the hydrocarbon backbone, and is a minor structural feature of monolayers. Many characterization techniques are not very sensitive to  $\phi$  on an individual monomer basis, and its relevance is not always perceived. However, it is logical to speculate that the rotation angle of each monomer may be different to facilitate the best possible packing under a regime of random head group adsorption.

The steric requirement of the functional groups supersedes that of the backbone in many SAM structures. The length of the hydrocarbon chain, as well as the molecular structure of the backbone itself, can also play a significant role in the

packing of a monolayer. For example, existence of other functional groups along the backbone or an aromatic backbone can obviously affect the spatial arrangement within the structure. In general, a long backbone in the monomer does not guarantee a dense SAM structure. The chain length has been shown to affect especially the tilt angle  $\psi$  [45]; see Fig. 2.2d). Regardless of the chain length, the mobility of monomers within the substrate plane is heavily limited by the substrate-head group interaction discussed previously, and the growth of the monolayer is quasi-epitaxial. Covalently adsorbed systems are formed on the basis of discrete, available sites; their structures follow the substrate morphology and are epitaxial by definition. It is clear that competing or complementary factors, and the exact interactions between a variety of head/tail groups, substrate, and backbone quickly complicate a theoretical approach to the structure. This leads to the experimental approach taken by many studies in the area. The ordered head group structures are the focus of many studies by traditional surface science methodology where a unit cell is considered to be the basic repeating element in head group packing. There are continuing studies regarding the exact nature of the size and orientation of a unit cell. Much more details can be found in [11]. The adverse spatial effect of substrate surface roughness is illustrated plainly in Fig. 2.2e). The packing structure is obviously weakened by the uneven placement of the head groups. This motivates the strict control of surfaces used in SAM formation. In order to minimize roughness and maximize available terraces on a given metal substrate, flame annealing or other heat treatment may be employed. These processes promote the reduction of the number of grain boundaries. Alternatively, thermal evaporated substrates are recommended over sputtered substrates (especially for Au), as the latter possesses a larger degree of roughness due to the larger kinetic energy in-



involved during deposition.

The temperature dependence of growth has not been thoroughly studied across many systems. A few investigations have found that there is a critical temperature ( $T_c$ ) for alkyltrichlorosilane SAM growth [46]. When prepared at a temperature lower than  $T_c$ , the monolayer assumes a denser packing; when  $T > T_c$ , the monolayer becomes disordered and exhibits diminishing coverage as  $T$  increases. Although it is logical to conclude that such a behavior is governed by the increased internal energy and hence extensible to other SAM systems, more detailed studies are required for a comprehensive picture of the temperature effect during growth.

The fact that it is relatively simple to perform the experimental procedures leading to SAM growth illustrates the robustness of self-assembly. However, caution should be taken to ensure that good quality samples are obtained.

## 2.4 Stability of monolayers

Practical application of SAM requires first the knowledge of the permanence of the structure. Here the stability of monolayers (especially octadecanethiol) is briefly described. In these discussions it is assumed that the initial SAM is of good quality, possessing dense packing and canted angle typical of the given system.

### 2.4.1 Thermal stability

In general, thermal effects on SAMs can be of two types: phase change (i.e. melting) and desorption. Akin to testing a load-cell in a tension test, increasing and then decreasing the ambient temperature (thus also the SAM temperature) gives a profile which characterizes the response, similar to that given by a strain

gauge/Wheatstone bridge. Much of the temperature-related data was collected using grazing-incidence X-ray diffraction (GIXD) [11]. During melting, the GIXD intensity response decreases as temperature increases; but the original value can be regained through cooling. Desorption, which occurs at higher temperature than that of melting, causes an irreversible intensity loss in GIXD measurement even upon cooling to the original ambient temperature. The melting temperatures of SAM systems are typically higher than the bulk melting point. This implies that the well-ordered monolayer structure is more stable, because the monomers are interacting more strongly than in bulk phases. For *n*-alkanethiol on Au(111), the melting temperature is around 100°C [23]. For octadecyltrichlorosilane, the melting temperature is 467°C [47]. At still higher temperatures, decomposition can occur and the monolayer will be disintegrated.

#### 2.4.2 Electrical stability

It has been demonstrated that electro-desorption of *n*-alkanethiol SAMs occur at a substrate potential of mere volts [48]. The desorption is a chemical reduction and the critical voltage is chain-length dependent: longer SAM requires a higher voltage to be desorbed. The electrical stability of other types of systems have not been thoroughly investigated. One expects that the substrate-head group interaction will be the determining factor in desorption, hence covalently bonded systems such as alkylsilane and alkyltrichlorosilane would have superior stability compared to *n*-alkanethiol when a potential exists in the substrate. Similar arguments, which favor the desorption of weakly interacting head groups, can be made with regard to other SAM systems.

### 2.4.3 Mechanical stability

Studies in vibrational damage or frictional wear on self-assemblies may seem inappropriate due to the reduced size of a SAM. Yet vibration and friction can also be described in a molecular sense. Vibrational damage is the collision of surrounding molecules with the monolayer. Similarly, friction can be described by the interaction between the molecules of two planar surfaces (e.g. SAM and another substrate). Recently, an investigation regarding vibration has been done with octadecanethiol. The treated substrate is immersed in the selected medium and ultrasonic vibration (38.5 Hz) is sent throughout the medium, causing cavitation damage [49]. The study confirms that poorly formed SAMs desorb within one to two hours under ultrasonic vibration. Well-formed SAMs are surprisingly immune to such vibration. An interesting result is that the canted angle inferred from FT-IR absorption spectroscopy is decreased (i.e. the monomers are more aligned with surface normal) after vibrational treatment. The precise mechanism of the effect requires future clarification. Tribological properties of SAMs in both macro-scale and micro-scale has been summarized [36]. Briefly, the friction coefficient of a surface can be dramatically reduced by SAM when the exposed chemistry increases hydrophobicity. With similar tail groups, coefficient of friction is lower on surfaces treated with long-backbone ( $C_{10+}$ ) SAMs when compared to treatment with monomers of short-backbone ( $C_2$  to  $C_8$ ). This is true of many monomer species, such as *n*-alkanethiol, fatty acids, and *n*-alkylsilane. Like many properties of SAMs, this difference between the tribological response of short/long chain length has also been attributed to the organized structure of SAMs [50]. Monolayers of short-chain monomers behave more like liquid-in-shear in these studies; the monolayers are also less durable to wear. Monolayers of long-chain monomers

are analogous to crystalline solid and have high durability.

## 2.5 DRW SAM systems

A number of SAM systems has been successfully used as the driving surface modification in DRW. These pairings are all capable of effecting hydrophobic surfaces in the short time allowed by the nature of the moving droplet. Specific characteristics of these surfactant-substrate pairings are discussed below. The pre-cursor liquid species is of paramount importance in a DRW system, as the fluid behaviors one studies follow directly from the solvent employed. In addition to having sufficiently large surface tension, solvents must also possess weak but sufficient solubility for the surfactant. In short, the choice of pre-cursor solvents are non-trivial; the solvent employed in each SAM pairing will be listed but not explored.

### 2.5.1 Primary amine on carboxylic acid tail-group

$[\text{CH}_3(\text{CH}_2)_n\text{NH}_2]$  in decahydronaphthalene on  $[\text{CH}_3(\text{CH}_2)_{15}\text{COOH}]$  (Au sublayer). The amine surfactant forms a Physisorbing layer above a grown SAM of mercaptoalkanoic acid. This is an example of the oriented, polar surfactant layer reported by Zisman [24]. In theory, the presence of the carboxylic acid monolayer is not required to grow the amine layer. The amine surfactants present a hydrophobic surface which has a decahydronaphthalene contact angle of approximately  $40^\circ$ , depending on the length of the backbone [51].

### 2.5.2 Perfluoroalkanoic acid on metal surfaces

$[\text{CF}_3(\text{CF}_2)_n\text{COOH}]$  in decahydronaphthalene has been observed to deposit hydrophobic monolayer films on Pt [24]. Alternatively Ti, Au, Al, and even bare silicon surfaces seem to be compatible substrates. This is also a Physisorbing,

polar monolayer. In all cases the kinetics this adsorption is very high. Even at low concentration (of order  $<1$  mM), the resulting modification may effect liquid wetting response in  $< 1$  seconds. The contact angles of liquids on these monolayers are high for even for hydrocarbons, which has low surface tension. A specific example is that of decane on perfluorolauric acid monolayer which produces the contact angle of  $70.0^\circ$ [52]. Although this modification is very effective in producing hydrophobic surfaces, it is not suitable for DRW research, primarily due to fact that its chemical kinetics far exceeds the relaxation of the fluid typically employed.

### 2.5.3 Trichlorosilane on glass

$[\text{CF}_3(\text{CF}_2)_n(\text{CH}_2)_m\text{SiCl}_3]$  in saturated hydrocarbon oil on glass. This is an example of chemisorbing SAM. Hydrosilylation of the trichloro-group with the exposed silicon on glass results in a strong Si-O-Si bonding of the backbone to the surface. Thus, the surface cannot be simply regenerated as in the case of physisorption. The chemical bonding does aid in SAM stability.

## 2.6 Summary

Self-assembly as a general class of thermodynamic / chemical equilibrium structures were discussed; the structure of self-assembled monolayers and some applications have been briefly reviewed. The substrate-head group interaction is perhaps the most significant factor in the formation and the resulting structure of self-assembled monolayers. In addition to its effect on the packing of SAMs, the interaction strength is also important in formation dynamics and the thermal, mechanical, or electrical stability of SAMs. A well-established procedure for solution growth of monolayers must consider factors such as the solvent,

monomer concentration, immersion time, substrate and monomer chemistry, substrate cleanliness, and substrate roughness. One has many instruments at his / her disposal to characterize the treated substrate, and a few of these methods have been outlined. Micro-Contact Printing has been discussed as an immediate application of SAM in designing surface characteristics. Over a hundred years since the works of Pockels, Rayleigh, Langmuir and others, self-assembly has moved from relative anonymity to the forefront of research. The application of the concept of self-assembly in biology, medicine, and other engineering disciplines is very promising.

## CHAPTER 3

### METHODS AND PROCEDURES

In this chapter the basic operation and setup employed in these studies will be outlined and elaborated upon. Experimental procedures are detailed, and the computer simulation technique developed is described. A general introduction to the Lattice Boltzmann Method employed is presented, with omission to the specific values of the parameters.

#### 3.1 Background on experimental approach

The generation of self-propelled drop movement, DRW, relies on the conversion of a high energy surface to a low energy surface that induces a change in wettability sufficient to provide the energetic driving force for drop movement. In the most commonly employed base surface (unless otherwise stated), the adsorption of a mercapto-alkanoic acid  $[\text{HS}(\text{CH}_2)_n\text{COOH}]$  onto gold generates a densely packed monolayer film that exposes carboxylic acid groups at its surface. These high energy surfaces are wet by most liquids including water. These surfaces could be modified by contact with a non-polar solution (decahydronaphthalene, DHN) containing an  $n$ -alkylamine. In this process, the amino group bonds non-covalently with the surface carboxylic acid group and generate an oriented monolayer of the alkylamine at the surface. The resulting bilayer exposes the methyl

groups ( $\text{CH}_3$ ) of the amines at its surface, as evidenced by its wetting properties by water and various hydrocarbon liquids. A treated surface is less wettable (i.e., exhibit higher values of advancing and receding contact angles) when alkylamines of longer chain lengths or solutions of higher amine concentrations are employed. Exposure of the bilayer to a polar solvent removes the amine layer and regenerates the high energy carboxylic acid surface. However, this regeneration is not considered complete as the contact angles may not return to the previous higher values. The adsorption process to generate the amine adlayer can effect a self-propelled drop movement on the carboxylic acid (high energy) surface. In general, any solution-surface pairing which results in the growth of an oriented, hydrophobic monolayer less wettable than the original surface is suitable for a DRW study. However, the extent of the motion depends heavily on the kinetics of the monolayer growth and the relaxation of the fluid to surface effects.

### 3.2 Solution process

The solution growth of hydrophilic, 16-mercaptohexadecanoic acid [ $\text{HS}(\text{CH}_2)_{15}\text{COOH}$ ] (90%, Aldrich) monolayer is performed with 200-proof EOH to result in ethanoic solution of the surfactants. A SAM sufficiently active for this DRW system can be achieved through a 5 minutes immersion of an active surface in 5 mM solution concentration. This immersion time is determined from a literature source which claimed that the percentage coverage of monolayer alkanethiolates is near completion (>80%) after 200 seconds [20]. An analogous process is performed to effect the growth of hydrophobic SAM of 1-octadecanethiol [ $\text{HS}(\text{CH}_2)_{17}\text{CH}_3$ ] (95%, Aldrich). A finished sample is first rinsed with washing alcohol (Fisher, 85% EOH and 15% methanol), then DIUF water (Fisher), and



dried with compressed (40 to 80 psi) nitrogen gas.

The amine (dodecylamine [ $\text{NH}_2(\text{CH}_2)_{11}\text{-COOH}$ ]; 90%, Aldrich) solution is prepared in DHN (also *decalin*, mixture of *cis/trans*, Aldrich) in various concentration, typically on the order of mM.

### 3.3 Micro-Contact Printing ( $\mu\text{CP}$ )

An immediate application of Self-Assembled Monolayers is for the modification of surface characteristics. With solution processes, a relatively homogeneous SAM can be grown over a large surface area. But it is more advantageous to have control over the local surface characteristic. For example, alternating regions of hydrophobic and hydrophilic nature may aid in the mixing of fluid streams in a micro-channel flow situation. A method that has been employed, in conjunction with SAM, to acquire such local surface design is Micro-Contact Printing. A comprehensive review of this and other similar methods, collectively known as Soft Lithography, can be found in the literature [53]. Due to the intrinsic randomness of the DRW motion, the possibility of surface wettability design is indispensable in creating a controlled experiment for the study of this system. In fact it is crucial in another, related application reported later.

Briefly, the  $\mu\text{CP}$  procedure is analogous to using a rubber stamp on paper. The components consists of a rubber stamp, an ink solution, and a surface. Yet contrary to conventional printing, where the ink is a colloidal suspension of any combination of pigments, not all SAM species may be used as ink in the  $\mu\text{CP}$  process. As a monomer species has its intrinsic directionality, a particular species cannot be employed for  $\mu\text{CP}$  if the inking process does not leave an inverted SAM on the stamp material. This is clearly illustrated in Figure 3.1. A silicon negative

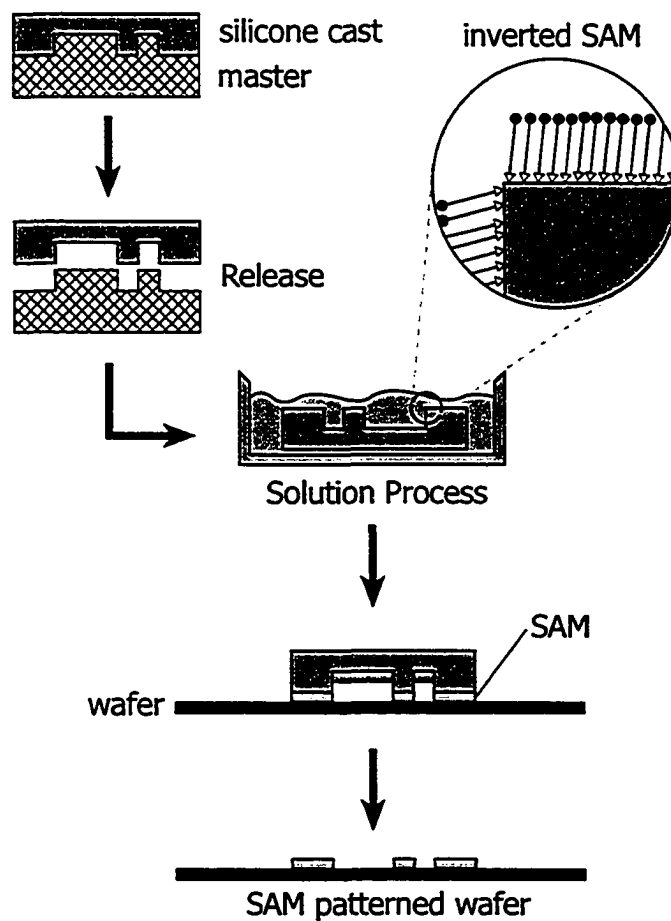


Figure 3.1: Flow-chart of the inverted SAM and the  $\mu$ CP process performed

of the rubber mask is first made by conventional photolithography to present surface relief. A silicone rubber is then casted against the negative. When cured, a physisorbing monolayer of the intended SAM species is formed on the stamp via solution growth. The stamp is then dried and presented, inverted, to the substrate. A short time is allowed for reaction and the stamp is released. The surface is thus left with SAM where the silicon negative is etched, and bare substrate material where the silicon negative is raised.

For these experiments, the silicon masters are based on  $0.6 \mu\text{m}$  silicon-dioxide covered wafers. Each design is produced by a pattern writer similar to those used for conventional CMOS processes with the lateral feature size of  $>1 \mu\text{m}$ . The designs are then exposed through UV photolithography, wet-etched and DRIE-etch in the BOSCH process [54] by an ICPRIE equipment within 24 hrs to ensure cleanliness. A 15 minutes piranha (3:1,  $\text{H}_2\text{SO}_4:\text{H}_2\text{O}_2$ ) immersion cleaning is occasionally performed for further removal of contaminants. Sylgard 184 silicone, obtained from Dow-Corning, is employed for casting. The silicone is cured under room temperature for at least 24 hrs, then released for use either immediately or within two weeks. The silicone stamp are reused for no more than 10 stamping processes, as the EOH immersion and other processes tend to introduce contaminants. The solution process for the growth of SAM on the silicone stamp is similar to that performed on a silicon wafer.

### 3.4 Experimental procedures and error estimation

The Discrete-drop Reactive Wetting experiment is performed on a smooth gold substrate prepared by the following procedures. A test grade silicon wafer of orientation  $\langle 100 \rangle$ , with a total thickness variation of  $<10 \mu\text{m}$ , is treated with

resistively evaporated metal flux under an ambiance of  $10^{-6}$  torr, resulting in a thin-film (100 nm) coverage of gold. The silicon wafer has a spot height variation of  $<10$  nm after this process and has been confirmed with Atomic Force Microscopy. The smooth sample surface ensures low contact angle hysteresis, so that the contact line may translate with the least possible resistance. Air-borne particulates on the surface were removed using pressurized, filtered nitrogen. A micro-contact printing technique [53] was first used to specify the hydrophobic regions; self-assembly of 1-octadecanethiol is employed for this purpose in conjunction with  $\mu$ CP. The remaining area on the gold surface is functionalized with 16-mercaptohexadecanoic acid to allow wetting by the droplets. A solution of dodecylamine in DHN (of various concentration as indicated in respective discussion) is employed for the liquid drop and its movement was recorded using a CCD camera (Sanyo VCB-3514) at 30 fps while positioned on a 3-axes micro-positioning stage. An additional, high-speed ( $>2500$  fps) CCD equipment (Redlake MotionPro) is employed when required. Both cameras are gray-scaled, and color additions in certain figures were achieved in post-processing.

The experiments are performed in open laboratory under atmospheric conditions. Drops of volume  $\sim 1 \mu\text{L}$  are deposited at one end of a COOH-exposing track/design using a micro-liter syringe and monitored. The drops move unassisted to the opposite end of the track. The temporal images are analyzed to recover the average position of wetting edges. The error in these position measurements can be estimated as the pixel width, which is of the order of  $\pm 0.5$  mm. Time measurement has the inherent frame speed error of approximately  $\pm 0.02$  second. Hence the length measurements are accurate to  $\pm 0.707$  mm, and the er-

ror in velocity calculations, in mm/s, are

$$\pm \left[ \frac{0.5}{x^2} + \frac{0.004}{t^2} \right]^{1/2} \quad (3.1)$$

where  $x$  represents the displacement in mm, and  $t$  the time elapsed in second. All static contact angle measurements are made using the Axisymmetric Drop Shape Analysis (ADSA-D) software [55], which determines the value digitally to within  $\pm 0.1^\circ$ . As these error are small in relative magnitude ( $\leq 1\%$ ), it is omitted in the discussion that follow.

### 3.5 Computational Method

The computer simulation of RW drop motion is performed using a two-component Lattice Boltzmann Method (LBM) which considers direct external rather than mean-field forces. Continuous flow simulation techniques such as the finite-element method (FEM) is unsuitable for this purpose. This is primarily due to a bottleneck in the translation of physical surface effects into boundary conditions sufficient for FEM. In addition, LBM relies on a density distribution instead of a sharp contact edge to describe the interface. Thus problems of the contact-line singularity and its derivatives which plague many contact line investigations can be avoided entirely in LBM simulations. I believe that the statistical nature of a reactive-wetting system is better simulated with an evolutionary dense-gas-automaton than a set of deterministic fluid equations. Modification was made in the LBM implementation to affect a transient wall density, simulating the first-order adsorption of hydrophobic surfactants. The lattice cells under study are cubic lattices with 19 discrete lattice velocities at each node; this is commonly designated in literature as D3Q19.

The LB method utilizes the equations

$$\begin{aligned} f_i^{\mathbf{a}}(x + \mathbf{e}_i \delta t, t + \delta t) &= f_i^{\mathbf{a}}(x, t) \\ &= \frac{f_i^{\mathbf{a}}(x, t) - f_i^{\mathbf{a},eq}(x, t)}{\tau_{\mathbf{a}}}, \end{aligned} \quad (3.2)$$

$f$  represents the number density distribution of the components in the cell, and the designations  $\mathbf{a}$  ( $= 1, 2$  or  $w$ ) represent the identity (fluid 1, 2, or wall, respectively) of the components.  $\mathbf{e}_i$  ( $i = 1 \dots 19$ ) represents the 19 lattice directions. The solid wall is attributed a density for the purpose of calculating the interaction strength. Equation (3.2) utilizes the BGK single-relaxation collision term which simplifies the known Boltzmann collision expression;  $\tau$  is the relaxation time. Expression for the equilibrium density distribution  $f_i^{\mathbf{a},eq}$  is lattice dependent to maintain material conservation. For a D3Q19 simulation this is:

$$f_i^{\mathbf{a},eq}(x, t) = \frac{n_{\mathbf{a}}}{W} \left( 1 + 3\mathcal{U} + \frac{9}{2}(\mathcal{U} \cdot \mathcal{U}) - \frac{3}{2}(u_{\mathbf{a}}^{eq})^2 \right) \quad (3.3)$$

$$\begin{aligned} n_{\mathbf{a}} &= \sum_i f_i^{\mathbf{a}}; \\ \mathcal{U} &= \mathbf{e}_i \cdot u_{\mathbf{a}}^{eq}; \end{aligned} \quad W = \begin{cases} 3 & \text{if } |\mathbf{e}_i| = 0 \\ 18 & \text{if } |\mathbf{e}_i| = 1 \\ 36 & \text{if } |\mathbf{e}_i| = \sqrt{2} \end{cases}$$

Similar expressions and derivations can be found in literature for other lattice geometry [56]. Briefly, this expression is the result of a single time relaxation (or BGK) factor that approximates the Boltzmann collision integral. Due to the simplicity of the BGK factor, the lattice cell can be conceptualized as a container in which particles collide and stream via discrete velocities to nodes in the lattice. The result of each collision is dictated by the method in which  $u_{\mathbf{a}}^{eq}$  is calculated. From Eq. (3.2) it is evident that the method is an evolutionary technique which

initiates itself with the results of the previous iteration. In this simplistic implementation, the simulations are initialized by a number density of  $n_a(x)$  associated to zero velocity in the entire cell. The behavior of the Lattice Boltzmann model has been scrutinized in literature and before simulation, trials that are designed to ensure the stability and the qualitative response of this implementation were also performed. The specific method used to recover the equilibrium velocity, and the verification trials will be described in relevant discussion.

## CHAPTER 4

### DEWETTING FROM HYDROPHOBIC SURFACES

Perhaps the first subject of importance to a DRW system is the motion away from a hydrophobic surface. After all, this particular tendency is the source of the drop motion. In this chapter, the motion of a droplet on a chemically heterogeneous surface is examined experimentally by subjecting the drop to gravity. The experiment is then parallel with a simulation, which shows a possible mechanism for liquid translation across chemical heterogeneity.

#### 4.1 Experimental perspective

To sufficiently measure the effect of surface gradient on dewetting, an experiment must be designed to result in varying degrees of hydrophobic modification. A horizontal drop-moving experiment will not suffice. This is because the motion of a drop is observed as soon as a sufficient hydrophobicity has been established, hence the surface left behind by the wetting front has only a minimal coverage. In reality, the bulk of the drop can be held back by a variety of factors and could refuse to advance: other, immobile contacting surfaces, air flow over the drop, and certainly, gravity.

One can thus create an antagonistic factor against dewetting by studying a climbing drop. In this case, the drop is forced to move up-hill against its weight.



Intuitively, a drop will slow down when subjected against gravity until the speed is zero; but this is not true with DRW. The drop advances with a constant, albeit lower, velocity. This lesser speed is essential in the investigation of dewetting from surface gradient. For the climbing drop, gravitational forces on the significant mass of the bulk gives a resistance to the motion of the ordered, interfacial region. Once overcame by sufficient surface gradient, however, gravity poses no difficulty to drop motion via reactive wetting, hence the constant velocity. A climbing drop experiment, conducted while holding all but the incline angle constant, is one that illustrates explicitly the dewetting of liquid from various surface gradients. Thus, the climbing drop in the following section.

## 4.2 Introduction

The motion of a three-phase contact line is an interesting and relevant area of current research. It is known that the three-phase contact line consists of a visible edge; if there is complete wetting it is led by a thin precursor whose height is hundreds of angstroms or less [3]. The spreading of the precursor precedes appreciable wetting hence motion in the contact-line. The complete wetting case proves to be more forgiving in formulation since a stress singularity occurs if one assumes zero fluid thickness at the contact line. The motion of contact line under transient circumstances where the contacted surface is under continuous modification, in other words, reactive, has also been known for a few decades. This excludes the Marangoni effect, which is a phenomenon in which the fluid density is transient depending on temperature. The solid surface modification is typically a molecular adsorption, forming self-assembled monolayers. The reactive version of the moving contact line problem involves wetting and dewetting of the fluid.

From a lubrication-type theory, the flow within such a drop has been proposed to be a superposition of shear flow and Poiseuille flow [2]. Recently, an atomistic account of wetting/dewetting flow has also been presented [5]. Where as a linear theory leads to symmetric dewetting and wetting (*i.e.* the response of the contact line is the same at both edges), it was shown that for a very small drop size significant evaporation at the dewetting edge, and condensation at the wetting edge; a rolling flow exists inside this liquid drop simulated by atomistic collisions. In addition to theoretical works, there has been a collection of experiments which induce translation of a discrete liquid droplet via a solid surface energy gradient [17, 57–59]. These experiments were carried out under atmospheric conditions on smooth substrates. The drop translates in an unpredictable manner, reflecting the intrinsic nature of the solid surface modification.

Using the reactive-wetting scheme, Chapter 6 will demonstrate the ability of manipulating discrete drops, as opposed to continuous-flow, for an alternative in microfluidic design [60]. In Lab-on-a-chip systems, which are typical microfluidic devices, continuous laminar flow is the dominant regime, and surface effects are significant due to the closeness of the bulk to interfacial regions. Instead of minimizing surface effects, the discrete-drop method utilizes functionalized surface in order to propel the liquid. The advantages of using discrete drops over continuous flow in microfluidics includes versatility in chip design and retention of sample concentration. It will also be shown in Chapter 6 that drop manipulation operations can be done separately to efficiently utilize the limited area available on a particular lab-on-chip substrate. Since the technique is immediately applicable to microfluidics, any contribution or detriment to the performance of the system is of great interest. Among many such factors, the effect of gravity is

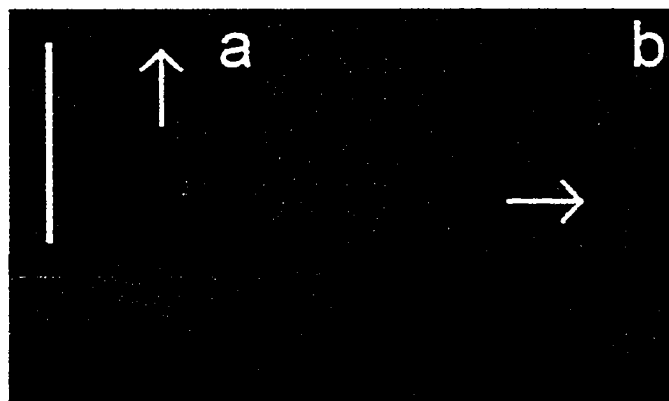


Figure 4.1: Captured image of: a) Top-view of the front and wake of a moving liquid volume under sufficient, rectangular wetting restriction; b) Macroscopic observation of the same liquid drop from the side; note that the reflection of the profile is also visible. The line in a) represents the length of 10 mm; b) is scaled differently.

more critical as the lab-on-chip device could be operated outside of laboratory conditions. The inclination in substrate may introduce fluid motion that deviates from design anticipations. The effect of gravity on the velocity of moving drops is thus an important issue. The nature of the motion of a three-phase contact line on reactive surfaces is also of fundamental importance to this study. There have been few specific investigations in the fluid interfacial flow of a reactive-wetting drop. An experimental approach would be difficult to reveal the flow information at the interface, leading to an unfruitful undertaking. Thus it is proposed to construct a computer simulation exhibiting accurate behavior of the liquid drop. In this way the simulation may elucidate the wetting and dewetting interfacial flows. The Lattice Boltzmann computation method was adopted. It is believed to be qualitatively reliable in understanding the behavior of a discrete liquid drops. This chapter summarizes such combined experimental and computational study of surface-ascending reactive-wetting (RW) drops against gravitational influence.

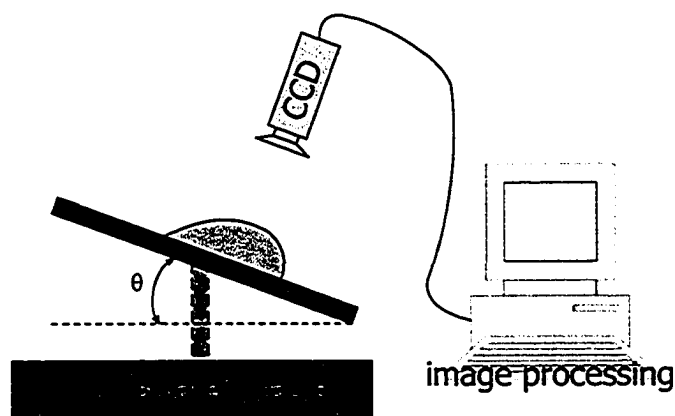


Figure 4.2: Schematics of the experimental setup. Note the CCD camera is aligned parallel to the substrate plane.

### 4.3 Procedures

#### 4.3.1 Experimental and Materials

The experiments were performed on smooth, flat gold substrates prepared by the following procedures. A test grade silicon wafer of orientation  $\langle 100 \rangle$ , with a total thickness variation of  $< 10 \mu\text{m}$ , is treated with resistively evaporated metal flux under an ambiance of  $10^{-6}$  torr, resulting in a thin-film (100 nm) coverage of gold. The silicon wafer has a spot height variation of  $< 10$  nm after this process and has been confirmed with Atomic Force Microscopy. The smooth surface ensures low contact angle hysteresis, so that the contact line may translate with the least possible resistance. Air-borne particulates on the surface were removed using pressurized, filtered nitrogen. A micro-contact printing technique [53] was then used to specify the hydrophobic regions; self-assembly of 1-octadecanethiol is employed for this purpose. The remaining area on the gold surface is functionalized with 16-mercaptohexadecanoic acid to allow wetting by the droplets. A 5 mM solution of dodecylamine in DHN was used as the droplet and its movement was recorded

using an aligned CCD camera at 30 fps. In each experiment, a  $2.0 \mu\text{L}$  drop of the DHN solution is deposited on a hydrophilic track under atmospheric conditions. The substrate is placed such that an acclivity is present against the direction of drop motion; see schematic diagram of Fig. 4.2. A general, captured image of a RW drop on zero ( $0^\circ$ ) slope is presented in Figure 4.1 to convey better understanding of the physical situation. The surface-ascension of RW drops were performed on a setup similar in function to the schematics of Figure 4.2. The substrate plane, or the incline of the solid surface, was measured by  $\theta$ . Between experiments,  $\theta$  was varied in increments of  $5^\circ$ . The trials were performed on a vibration-isolated air-table. A CCD camera captured the experiments at 30fps in gray-scale for image analysis. The camera was carefully aligned with the substrate to minimize distortion.

### 4.3.2 Computer Simulation

The general computational scheme has been described in Chapter 3. The lattice cell under study is  $50(X)$  by  $20(Y)$  by  $20(Z)$  units in size with 19 lattice velocities (D3Q19). The cell was subjected to periodic boundary conditions in the  $X$  and  $Y$  directions; bounce-back boundaries were implemented at  $Z = 1$  and  $Z = 20$ . The plane of  $Z = 20$  was treated so that surface interactions were omitted.

A typical simulation is initialized using a previously equilibrated hemispherical drop of approximately 14 lattice-units in diameter and a contact angle of approximately  $57^\circ$  by the tangent line method. The initial drop was brought to an equilibrium without solid surface interactions so as not to introduce bias into its density distribution. The density is taken after approximately 1000 steps and then employed for all subsequent simulations of surface-ascending drops. In the com-

puter study, the substrates were also deviated from the horizontal position in  $5^\circ$  increments. To effect reactive-wetting, the wall node densities ( $n_w$ ) in simulation are modified by the following equation:

$$n_w = H \left\{ 1 - \exp\left(\ln\left(1 - \frac{n_w}{H}\right) - k\right) \right\}. \quad (4.1)$$

$H$  is the surfactant-dependent hydrophobic limit,  $k$  is the parameter determining the rate of adsorption. The density increases with simulation time in which the node is exposed to sufficiently dense liquid, giving a first-order response. The strengths of interaction, whether solid-liquid or liquid-liquid, are adjusted through multiplicative parameters  $g_{ab}$ :

$$F_a(x) = n_a \sum_{x'} g_{ab} n_b(x') (x' - x), \quad (4.2)$$

where  $a$  and  $b$  indicate the identity of the fluid component or wall node. The effect of gravity is implemented in a similar fashion using the parameter  $g$ , affecting only fluid components but not the wall nodes. In this study, the parameters were as follows:  $\tau = 1$ ;  $g = 7.5 \times 10^{-5}$ ;  $g_{12} = 0.02$ ;  $g_{1w} = g_{2w} = g_{11} = g_{22} = 0$ ;  $H = 0.35$ ; and  $k = 0.01$ . The average number densities of fluids 1 and 2 were of the order of 1.

## 4.4 Results

### 4.4.1 Experimental Results

The ascension of a liquid drop against gravity is shown in Figure 4.3. Note that the general motion of such a drop is similar to that of a drop moving on horizontal plane. A wetting (front) with approximately constant geometry precedes a dewetting (wake) edge, whose contact line is transient. The dynamic contact

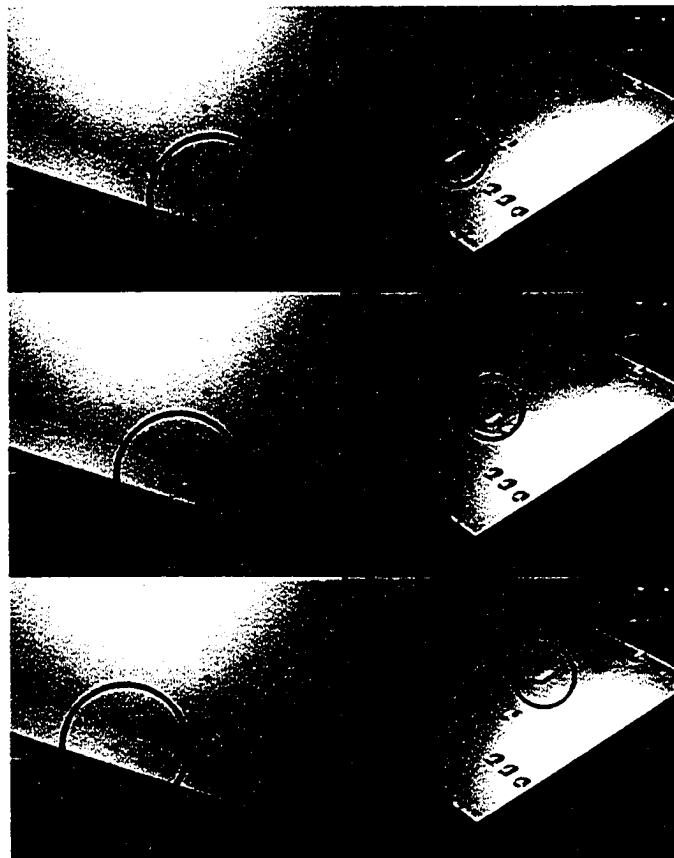


Figure 4.3: The captured images of a surface-ascending liquid drop in two proof of concept experiments. The circles in each picture highlights the location of the drops, which can be seen to move to a higher position from a previous picture.

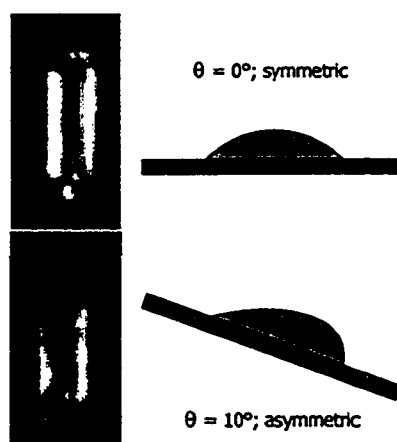


Figure 4.4: Schematic and captured image of asymmetric longitudinal profile; a horizontal case is provided for comparison.

angles differs, with the advancing angle being slightly smaller than the receding angle. These values cannot be predicted through Young's equation, Eq. (1.5). As expected for a drop under body-force, the empirical, longitudinal drop profile is asymmetric. Figure 4.4 provides the schematics and the light-enhanced images of an ascending drop supporting the schematic diagram. It is evident from these figures that the profile of a drop under gravitation in the non-normal direction is altered. This has unforeseen consequences for the velocity of the drops. Complementary to change in drop profile, the phenomenological length of a drop in the hydrophobic track also varies from the horizontal case. In these trials, the case where the substrate acclivity were  $10^\circ$  and  $15^\circ$  are worth noting and will be discussed following an account of the velocity of the drop.

It is perhaps surprising to note that the velocity with which a RW drop climbs is constant. This is a clear result from the time-sequence photography and not a conclusion deduced from observation of the naked-eye. The hysteresis of contact angle in these experiments is negligible, and cannot effect the gradual slow-down



normally observed in a descending rain-drop on, for example, a windshield. The constant velocity can be attributed to the fact that the RW phenomenon is a dynamic equilibrium state. The phenomenological velocity is the balanced result of the effects from liquid dewetting, surfactant adsorption, and gravity. Intuitively, a significant decrease in speed is produced from an increase in the slope of the substrate plane, and vice versa; see Figure 4.5. Dewetting of the three phase contact line is inhibited through surface tension by the bulk of the drop, which is in turn affected by gravitation on a slanted plane. The maximum, or stopping, angle at which a 2  $\mu\text{L}$  drop may climb spontaneously is  $>25^\circ$  as implied in Fig. 4.5; at higher slope the drop is unable to ascend.

To gain a better understanding of the velocity trend, it is assumed that the volumetric flow rate,  $Q$ , of an ascending drop is

$$Q = Q_0 - Q_g. \quad (4.3)$$

$Q_0$  and  $Q_g$  are respectively volumetric flow rate due to surface and gravitational effects. Since the drop is constrained by rectangular hydrophobic tracks and its profile is approximately constant through its ascent:

$$v = v_0 - v_g. \quad (4.4)$$

By definition,  $v_0$  is the velocity of the drop on the track due to dewetting flow and hence the velocity exhibited when the incline is  $0^\circ$ .  $v_g$  is a velocity due to gravity. As gravity is a body force acting on the entire drop, it is reasonable to argue that

$$v_g \propto C \cdot g \sin \theta. \quad (4.5)$$

The coefficient  $C$ , however, cannot be sought exactly due to the randomness in

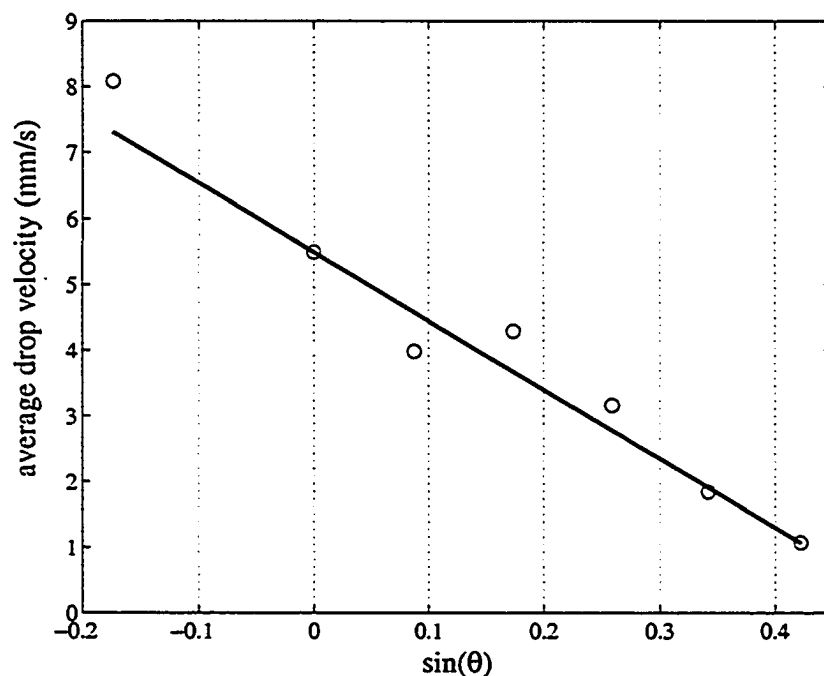


Figure 4.5: Experimental velocity of the surface-ascending drops. Linear least-square regression gives  $v = 5.49 - 10.462\sin\theta$ , with an  $R^2$  value of 0.95

surface wetting characteristic and the transience of in drop profile. Using the assumed relationship of  $v = v_0 - C \cdot g \sin\theta$ , a good fit to the experiment is generated as shown in Figure 4.5; in this case  $C = 1.07$ . The stopping angle, as predicted by this relationship, is  $31.63^\circ (>25^\circ)$ . This is in accordance with the experimental result.

There is now an opportunity to discuss the  $10^\circ$  and  $15^\circ$  cases. It has been reported that the antagonistic shear flow at the surface may increase when the longitudinal length of the drop is large, causing longer drops to move more slowly [61]. Specifically, an optimal length (usually predicted at the capillary length) can be found if the surface is positioned horizontally. For the specific system of dodecylamine in DHN on carboxylic acid monolayer employed, it is found that

this empirical optimal length is approximately 3.5 mm. The average length of an ascending drop against a  $10^\circ$  incline is 3.08 mm; that against a  $15^\circ$  incline is 3.84 mm. The positive deviation seen in the  $10^\circ$  case (see Fig. 4.5) is due to a smaller shear flow, which in turn is the result of the short drop length. One cannot expect to employ the optimal length exactly in the more complex situation with gravity under consideration. But the  $10^\circ$  and  $15^\circ$  cases obviously are situations when the reduction in shear flow is significant. The reduction in length is a simple effect of the surfactant adsorption. It is assumed that an amine monolayer of approximately homogeneous wetting characteristic is left behind the trail of a reactive-wetting drop. Since the velocity of an ascending drop is smaller than that at horizontal plane, the amine monolayer coverage would be greater and hence the contacting surface has lower energy. Less wetting of the wake (dewetting) edge is thus observed from shorter length of the drop. Thus the observed trend is that increase in substrate plane causes decrease in drop length.

#### 4.4.2 Computational Results

Before simulation of any surface-ascending drops, it is prudent to confirm that a simulated liquid drop does not display longitudinal motion save perhaps spreading when a simulated adsorption is omitted from the implementation. This is shown in Figures 4.6. In these two simulations the substrate plane is  $0^\circ$ , and the bottom solid surface is set to a given surface energy. In terms of wall node density,  $n_w$ , the values used in Fig. 4.6a) and b) are 0.35 and 0, respectively. Spreading, complete wetting, and coalescence is observed in Fig. 4.6b); dewetting and a high contact angle signifying a low surface energy in Fig. 4.6a). In both simulations the drop does not display appreciable motion from its initial position. Thus any translation

of the drop in the simulations is due to gravity, simulated surfactant adsorption, or a combination of those factors. In many of the simulation results presented, a roll-shaped drop is visible on the top surface of the simulation cell; see for example Fig. 4.6b). This is simply a condensed drop due to the bounce-back boundary condition on the particular surface. It is reasoned that due to its appreciable distance, this condensate does not significantly affect the liquid drop under study. This will become clear once it is shown in a later figure that the mass-flow in the volume between the liquid drop and the condensate, generally larger than 7 lattice units in height, is nearly zero. The simulation of a drop against a  $10^\circ$  incline is employed as an exemplary case in most of the discussion that follows for the sake of consistency.

In Figure 4.7 an example of moving liquid drop via LBM simulation is shown. As it is evident from the figure, the velocity of the drop is constant, similar to the RW drops in experiments. As it is difficult to translate the parameters used in a LBM simulation to exact physical quantities, the gravitational forces is adjusted through the parameter  $g$  until it is comparable to the effect of hydrophobic surface forces. The resulting parameter ( $g = 7.5 \times 10^{-5}$ ) is three magnitudes smaller than the fluid intermolecular interactions ( $g_{12} = 0.02$ ), which would be electrostatic in nature. This is physically correct as gravitational force is in reality magnitudes smaller than forces of an electrostatic origin. Since the LBM simulations generate drops with an average interfacial thickness of one to two lattice units, the volume of the simulated drops are in principle very small. This is also reflected from the dynamic contact angles exhibited by the LBM-simulated drop, which does not compare to experiments such as Fig. 4.3. Digressing briefly, Figure 4.8 shows the simulated surface energy, hence wall node density, of the solid surface support-

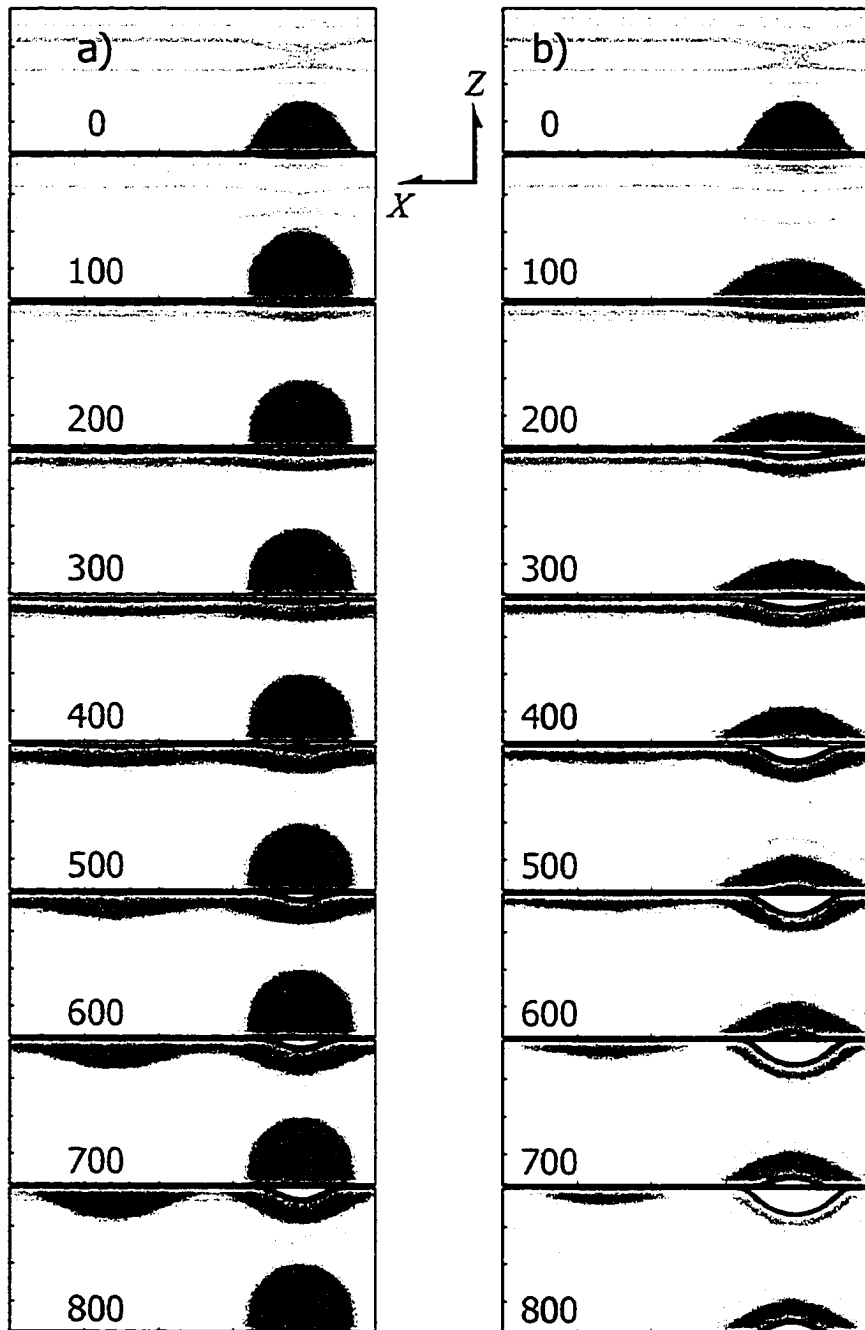


Figure 4.6: LBM simulations of static drops with each frame separated by 100 simulation steps. The substrate plane is horizontal in both cases. a) low energy surface b) high energy surface

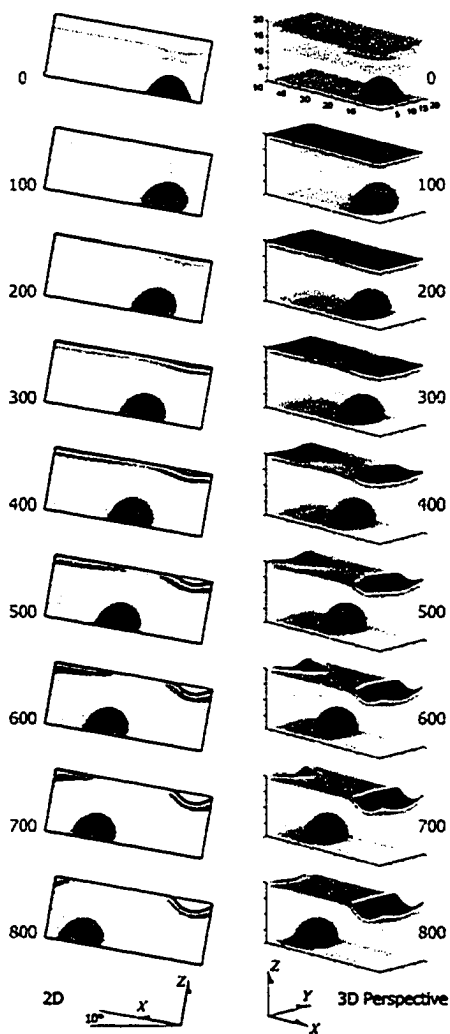


Figure 4.7: LBM simulation of an ascending drop with each frame separated by 100 simulation steps. The incline is  $10^\circ$ . Each frame of the two-dimensional view has been rotated by the incline angle to convey better understanding. A three-dimensional view is provided for comparison.

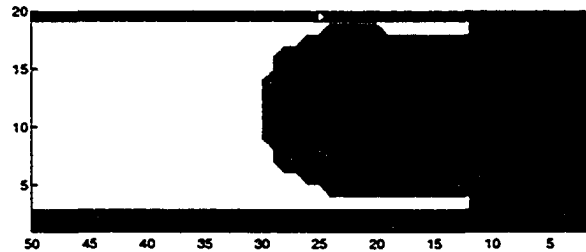


Figure 4.8: The hydrophobicity of the solid surface ( $XY$  plane at  $Z = 1$ ) supporting a surface-ascending reactive-wetting drop; substrate plane is  $10^\circ$ .

ing the drop. One can immediately confirm from Fig. 4.8 the assumption that a surface which has supported RW drop has a homogeneous wetting characteristic. There are very small differences between the average values of wetted wall node density for various substrate acclivity. The lack of length variation in the simulated surface-ascending drops lead to this difference. This situation can be remedied by adjusting the rate of simulated adsorption through the parameter  $k$ . Analogous to actual experiments, the relation  $v = v_0 - C \cdot g \sin \theta$  is also employed in obtaining a regression of the simulated ascending velocities. This is shown in Figure 4.9. The simulated results are in good agreement with the regression with a coefficient ( $C \cdot g$ ) of 0.0441. It is interesting to note that this relation predicts that there is no stopping angle for the particular drop size. It is inferred from this fact that a small drop may climb vertical substrates. In fact, it has been observed in experiments that small droplets with volume of the order of  $nL$  can ascend substrates positioned vertically. Therefore, it is concluded that the general behavior of the LBM simulations mirrored those observed in experiments and the predictive

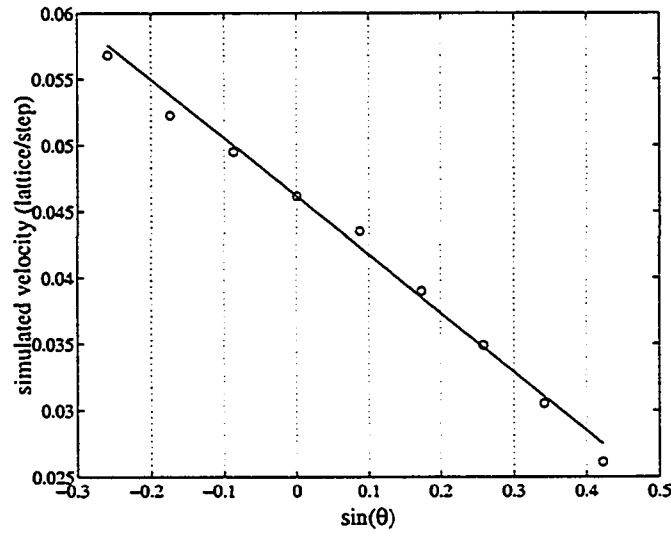


Figure 4.9: Climbing velocity from LBM simulations. Least square regression is also plotted ( $v = 0.0462 - 0.0441 \sin \theta$ ) with a  $R^2$  value of 0.99.

employment of LBM on reactive-wetting systems is qualitatively reliable.

The above shows that the general translational behavior of a surface-ascending, RW drop can be produced via LBM. In order to gain further insights in the fluid transport of reactive-wetting, the mass-flow field of such a drop from the simulation can also be examined. Figure 4.10 shows the streamline of a  $XZ$  plane-section within the simulation cell. Figure 4.11 shows a collection of cross-sectional velocity plots of the mass-flow field in the simulation cell. The incline is again  $10^\circ$  in both figures. Note that there are large volumes of the simulation cell which has very small mass-flow. From Fig. 4.10 it is also evident that a plane exists outside of the condensate which carries the mass flow downstream; in other words, the condensate only captures or releases fluid mass by evaporation and condensation. These two facts support the earlier claim that the condensate drop on the top surface of the cell does not interfere with the proposed investigation through flow or pressure. In each cross-section in Fig. 4.11, mass-flow in



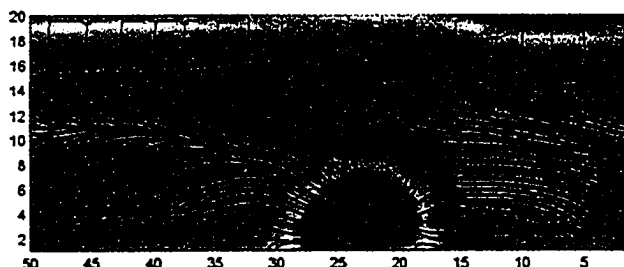


Figure 4.10: Streamline of a surface-ascending drop via LBM simulation; this  $XZ$  plane is given at  $Y = 10$  and intersects with the center of the drop.

the direction normal to the section is indicated by color as shown on a color-bar. Density plots of the fluid are provided for positional comparison. It is important to note that this flow information is difficult to obtain experimentally even with a fluorescent agent, and it reflects one possible route which a fluid undertakes to result in an observable reactive-wetting. Similar flow patterns were obtained from the LBM simulation of RW drops on horizontal substrates.

Fig. 4.11a) and c) show that the solid-liquid interfacial mass-flow can be described as follows. The solid surface under the drop is under continual surfactant adsorption that modifies its hydrophobicity. The more hydrophobic surface under the drop contributes to a upward flow away from the bulk of the moving drop, in this case toward the back of the drop. The more hydrophilic surface, having less surfactant coverage, also induces a upward (albeit smaller) flow away from the bulk, toward the wetting edge of the drop. To extract further information, the pressure within the lattice cell in simulation is also plotted in Figure 4.12. The negative number signifies expansion/evaporation, and positive values represents

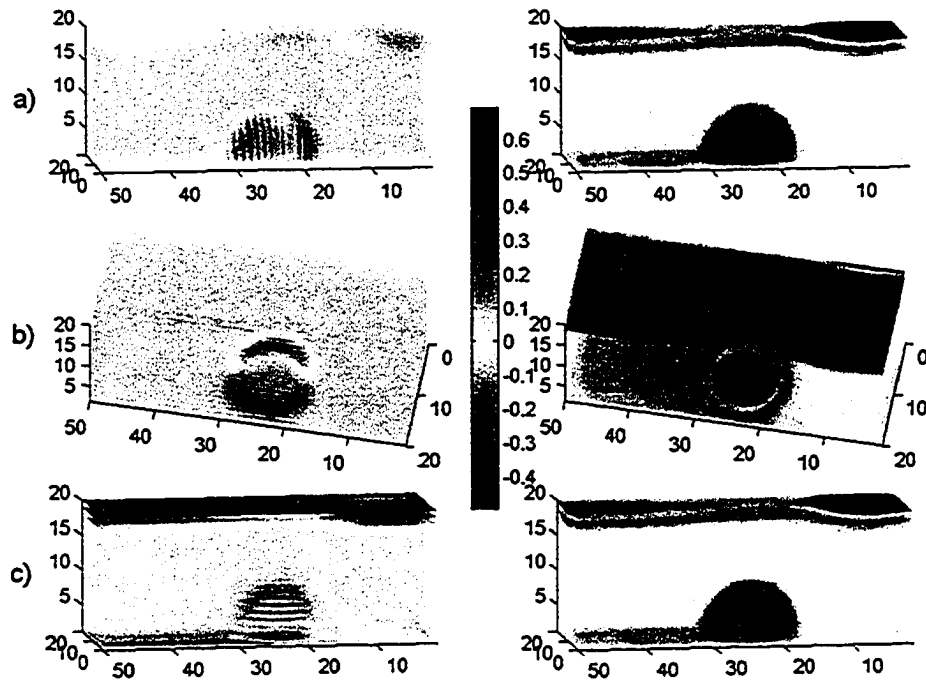


Figure 4.11: Slices of the mass-flow field of an ascending drop against an incline of  $10^\circ$ . Part a) shows cross-sections with constant  $X$  values; part b) with constant  $Y$  values; and part c) with constant  $Z$  values. Each slice shows only the flow normal to its plane, and the direction is indicated in color: blue represents the positive and red is the negative direction. White represents stagnant flow. Density plots similar to Fig.4.7 is provided for the purpose of position comparison.

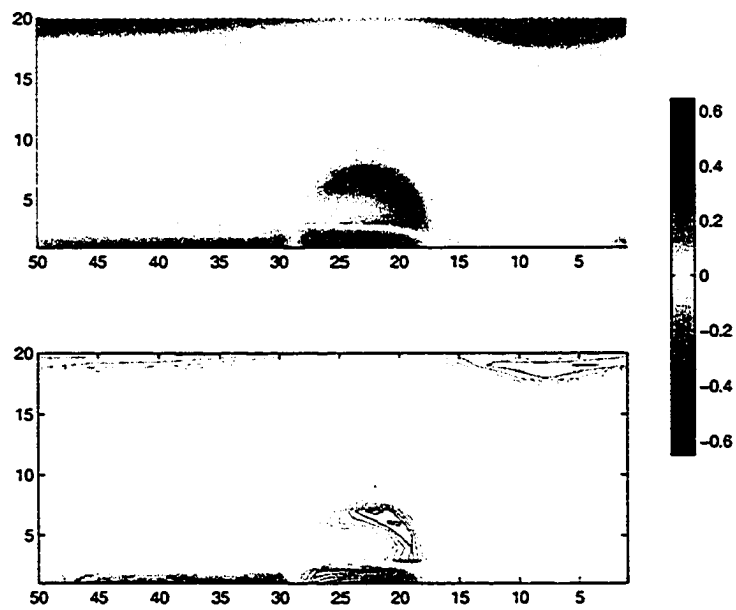


Figure 4.12: Pressure in a surface-ascending liquid drop through LBM simulation, obtained through material derivative  $D\rho/Dt$ .

compression/condensation. It is obvious from Fig. 4.12 that condensation occurs at the solid-liquid interface, more so at the front than at the wake of the drop. Evaporation occurs in the rear-portion of the drop, which I call the "cap". Employing these figures (Figs. 4.10, 4.11, and 4.12), it is convenient to summarize the nature of a reactive-wetting drop from a LBM simulation. The cap evaporates and moves toward the rear of the drop. Captured by surface tension, this mass flow drives the majority of the drop mass forward in the  $X$  direction, which is the main contribution to the visible translation of the drop. As gravity is a body-force, it contributes to a flow of the entire cell in the antagonistic direction, thus slowing the drop. Contrary to predictions of the lubrication theory or that from an atomistic evaluation, no rolling flow is found within the RW drop in a LBM simulation. In addition to velocities in the longitudinal direction, there is also a significant lateral movement in the drop, whose effect is to widen the span of the drop; see Fig. 4.11b). This is in fact an experimentally observable effect and further attests to the accuracy of LBM simulation. Overall, the motion of a RW drop is due to the transport of fluid in the interfacial region, which in turn drives a bulk flow that pedestals on the interface. This is markedly different than that previously proposed by some authors on similar subjects (for example [2],[4]). The RW scheme is non-continuous in the sense that it is not strictly momentum-driven. Thus treatment of the problem using Newtonian dynamics may not yield an accurate description.

#### 4.5 Summary

These results lead us to the clear conclusion that the substrate plane of a microfluidic device employing discrete drops should be carefully designed to account for

acclivity or declivity during operation. A discrete, reactive-wetting drop behaves differently when subjected to gravitational forces in the direction of its motion. The effect of gravity can be obviously made negligible through a reduction in drop volume. The nature of fluid flow in such a moving drop is also demonstrated using Lattice Boltzmann simulation of the ascending drops. A large portion of the drop is driven by the small interfacial transport, which accounts for the significant effect of a volumetric force such as gravity on the reactive-wetting system.

### **Acknowledgments**

I gratefully acknowledge financial support from the Alberta Ingenuity through a studentship grant for this work.

## CHAPTER 5

### LENGTH TO VELOCITY RELATIONSHIP

It is now clear that liquid droplets can be made to self-propel by the generation of a surface gradient on a supporting substrate *ex situ*, as recently demonstrated [58]. With respect to the progressive generation of surface energy gradient, Dos Santos and Ondarçuhu conducted experiments using 1H,1H,2H,2H-perfluorodecyltrichlorosilane surfactant solutions (in octane) on glass substrate [57]. Lee *et al.* employed an independent setup of octadecylamine surfactant solution (in decahydronaphthalene) on alkanethiol/gold substrate [17]. Given the similar nature of the two experiments – both actively produce a surface energy gradient to propel the carrier liquid – one would expect a unifying trend in a droplet length versus velocity relationship for these separate solution-substrate systems.

Intuitively, viscous shear drag at the droplet-substrate interface increases when a longer droplet is employed, leading to a decrease in droplet velocity. This trend has indeed been reported by Lee *et al.*. However, experimental results from Dos Santos and Ondarçuhu were contradictory. These authors observed an increase in droplet velocity as they employed longer droplets. The two groups of authors also employed different descriptions to quantify their experiments. There is a need for an overall description of the length/velocity relationship, which could explain both of the previously studied cases simultaneously. In this chapter, the

chemical influences on whether a given reactive wetting system should be treated by a kinetic or equilibrium approach is examined. It is of interest to note that the terminology of *equilibrium* and *kinetic* is used loosely here to identify the degree to which the chemical process, or adsorption, effect the velocity of a droplet. It is not to indicate the transitory nature of the system. Given the discussion in Chapter 1, a lubrication theory approach will be taken to illustrate the application of classical theory on DRW.

## 5.1 Empirical relations

### 5.1.1 Force balance

Both groups of authors observed that the velocities of the droplets were constant, suggesting force balance during motion. Starting with the simple notion that viscous-shear force  $F_v$  and unbalanced surface force  $F_Y$  are the only forces involved in the system, then  $F_v = F_Y$ . An expression for the unbalanced surface force can be obtained using classical Young's equation [55] at both advancing and receding edges of the moving droplet, if the drop is considered quasi-static. Thus write the unbalanced surface force is

$$F_Y = \gamma_{lv}(\cos \theta_a - \cos \theta_r) \quad (5.1)$$

where  $\gamma_{lv}$  is the liquid-vapor interfacial tension;  $\theta_a$  and  $\theta_r$  represent the contact angles of the advancing and receding edges, respectively; because of the nature of the reactive wetting mechanism considered,  $\theta_a < \theta_r$ . The expression for viscous-shear drag can be derived directly from Navier-Stokes momentum equations [62] assuming flow in two dimensions. Let us consider  $x$ ,  $z$ , and  $v$  as the horizontal axis, vertical axis, and velocity profile inside the droplet, respectively; the sup-

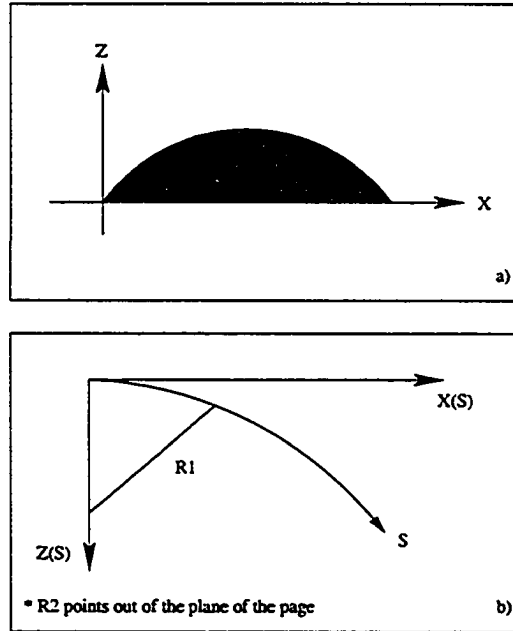


Figure 5.1: Schematics of the coordinate systems used in lubrication approach.

porting substrate as the datum/zero for  $z$  axis (see Fig. 5.1a).  $\zeta$  represents the height profile of the droplet along its length and  $\mu$  for the viscosity of the liquid. Employing boundary conditions  $v|_{z=0} = 0$  and  $dv/dz|_{z=\zeta} = 0$ , the following expression for  $v(z)$  is obtained:

$$v(z) = \frac{dP}{dx} \cdot \frac{z^2 - 2z\zeta}{2\mu} \quad (5.2)$$

where  $P$  is the pressure inside the droplet. To obtain the value of  $dP/dx$ , the velocity profile  $v(z)$  is expressed as a differential of fluid flux at any position  $x_0$  with an average droplet velocity  $V$  in the  $x$  direction:

$$V\zeta(x_0) = \int_0^{\zeta(x_0)} v(z) dz \quad (5.3)$$



The pressure gradient can then be written as  $dP/dx = -3\mu V/\zeta^2$ . Hence the velocity profile  $v(z)$  and shear force  $F_v$ , respectively, is:

$$\begin{aligned} v(z) &= \frac{3V \cdot (2z\zeta - z^2)}{2\zeta^2} \\ F_v &= \int \mu \frac{dv}{dz} dx = 3\mu V \int \frac{dx}{\zeta(x)} \end{aligned} \quad (5.4)$$

Equation 5.4 is in a known form of the lubrication approximation. Its applicability to the moving-drop problem depends on the validity of the boundary conditions. For the droplets in consideration, the dimension of the system is much larger than micrometers, hence slippage is not significant compare to the bulk. It is also reasonable to assume  $dv/dz$  at the liquid-air interface is zero, which ensures the time-invariance of the interface line. Equating  $F_v$  and  $F_Y$  yields

$$3\mu V \int_a^b \frac{dx}{\zeta(x)} = \gamma_{lv}(\cos \theta_{adv} - \cos \theta_{rec}) \quad (5.5)$$

The limits 'a' and 'b' of the above integration refer to either contact edge of the droplet at the substrate. Equation (5.5) assumes two dimensional flow, thus droplet length becomes the only important droplet-size-dependent variable that affects both  $F_v$  and  $F_Y$ . These two forces are treated separately in the following sections.

### 5.1.2 Viscous force dependence on drop length

As the droplet increases in length, its contact area increases and height profile of the droplet varies. Since the droplet is in motion, the definition of viscosity depicts that velocity profile along its height at a given position determines the shear stress at that discreet position. The total viscous-shear force then depends on the cross-sectional shape of the droplet, hence left-hand-side of Eq. (5.5). First, assume that drop length is below or sufficiently close to its capillary length  $\lambda^{-1} = (\rho g/\gamma_{lv})^{1/2}$ .

Through pressure equilibrium, the droplet shape is accessible using the Laplace equation of capillarity [55]:

$$\Delta P = \gamma_{lv} \left( \frac{1}{R_1} + \frac{1}{R_2} \right) \quad (5.6)$$

where  $\Delta P$  is the pressure difference across the liquid-vapor interface;  $R_1$  and  $R_2$  are the two principal radii of curvature. Again using the  $x$  and  $z$  coordinates, but redefining the  $z$  datum at the apex of the droplet (see Fig.5.1b). Equation (5.6) can be reduced to a system of differential equations:

$$\begin{aligned} \frac{d\phi}{ds} &= 2b + Cz - \frac{\sin \phi}{x} \\ \frac{dx}{ds} &= \cos \phi \\ \frac{dz}{ds} &= \sin \phi \end{aligned} \quad (5.7)$$

where  $C$  is the capillary constant, defined as  $\rho g / \gamma_{lv}$ ;  $b$  is the curvature at the apex of the droplet;  $\phi$  is the tangent at any point on the parametric curve  $s$ . The Laplace equation of capillarity is suited to approximate the location of the interface between two phases, and this formulation is especially suitable for smaller droplets where gravity is negligible. The droplet is assumed to be axisymmetric as the difference between the advancing and receding contact angles is small. The boundary conditions  $x(0) = z(0) = \phi(0) = 0$  is applied; by definition,  $d\phi/ds|_{s=0} = b$ . In two dimensional flow, the term  $(\sin \phi/x) \rightarrow 0$  as  $R_2 \rightarrow 0$  in Eq. (5.7). To further simplify the system, it is assumed that  $\phi(s)$  has an absolute value smaller than 1 radian ( $57.3^\circ$ ) over the length of the sessile droplet and obtain the estimation for  $\phi(s)$

$$\phi(s) = \frac{b}{\epsilon} \sinh(\epsilon s) \quad (5.8)$$

where  $\epsilon^2 = \rho g / \gamma_{lv}$ . Simultaneous integrations yield the location of the parametric curve:

$$\begin{aligned} x(s) &= \int \cos\left(\frac{b}{\epsilon} \sinh(\epsilon s)\right) ds \\ z(s) &= \int \sin\left(\frac{b}{\epsilon} \sinh(\epsilon s)\right) ds \end{aligned} \quad (5.9)$$

Equations (5.9) were used to numerically generate complete Laplacian curves, and the values of  $\int_a^b dx / \zeta(x)$  required in Eq. (5.4). The effect of length on viscous-shear drag can be thus shown. It will be shown that the intuitive result — length increase leads to viscous drag increase — is correct.

### 5.1.3 Adsorption reaction dependence on drop length

The effect of droplet length on adsorption can either be positive or negative, depending on the adsorption system in question. As droplet length and the associated contact area increase, more sites become available for adsorption. Contact area increase corresponds to longer contact time between the adsorbate-carrying liquid and substrate, hence a positive effect on the percentage of adsorbate coverage  $x_c$ , surface energy gradient, and eventually droplet velocity. However a limit must exist beyond which increase in contact area has no additional effect on the adsorption reactions, hence equilibrium. Furthermore, an excessive length can result in large viscous-shear drag, as discussed above. Thus it is speculated that the effect of adsorption reaction may eventually become negligible, and  $(\cos \theta_a - \cos \theta_r)$  in Eq. (5.5) is approximately constant.

Brochard-Wyart and de Gennes [63] commented on Dos Santos and Ondarçuhu's experiments, and described the adsorption mechanism as a first-order kinetic pro-

cess:

$$x_c = 1 - \exp\left(\frac{-kcL}{V}\right) \quad (5.10)$$

Lee *et al.* [17] employed a Langmuir isotherm to describe the adsorbate coverage at equilibrium condition as

$$x_c = \frac{Kc}{1 + Kc} \quad (5.11)$$

In the above equations,  $x_c$  is the percentage of adsorbate coverage,  $k$  is the kinetic rate constant,  $K$  is the adsorption constant,  $c$  is the adsorbate concentration and  $L$  is the drop length. Both of these descriptions worked well within the framework of their respective experiments. Yet neither description is able to predict the contrasting trends in velocity between the two systems. Here a transition for the separate experimental systems is proposed — where the suitable description of velocity shifts from kinetic to equilibrium or vice versa. Qualitatively speaking, the two descriptions above provide the ideal case studies of the length/velocity relationship. Since rate description Eq. (5.10) is likely to dominate when the viscous force is small, this description is more accurate at smaller lengths. Similarly, the equilibrium description Eq. (5.11) is expected to be true at larger lengths, where the viscous-shear force is much larger compared to the increase in unbalance surface force due to higher adsorbate coverage.

## 5.2 Results and Discussion

### 5.2.1 Methods

The numerical calculations employed are briefly described here. In previous sections, the Laplacian curves is mentioned in order to calculate the profile-dependent integral in Eq. (5.5). Romberg integrations were used to quickly obtain O(6) estimations to Equations (5.9). Tabulated data from Hartland and Hartley [64]

suggests that  $b$ , the apex curvature, can be used as a parameter to obtain a series of Laplacian curves. Contact angles for each profile were kept constant using a second-degree polynomial fit to the generated Laplacian curve. For the value of integral  $\int dx/\zeta(x)$ , there are possibilities of division-by-zero at each edge of the droplet where the height is, by definition, zero. The truncated height profiles are employed to estimate the integral values.

### 5.2.2 Combined description of the two adsorption experiments

First, one must test the hypothesis that reaction mechanics may be neglected at some length scales. For the  $n$ -alkylamine(DHN)/thiol/gold system, the numerical solutions using Eq. (5.5) do not fit the experimental data well when reaction effects are neglected ( $\cos \theta_a - \cos \theta_r$ , assumed constant), as evidenced in Figure 5.2. It is concluded that the reaction mechanics must be taken into account. It is interesting to note that the early attempts by using qualitative polynomial approximations of droplet profiles, which had little physical relevance, was successful to obtain a fit to this same set of experimental data (also neglecting reaction effects). The necessity of the Laplacian curve calculation is emphasized here — one needs to perform the more accurate Laplace solution for droplet cross-section profile in order to avoid misleading results. For adsorption of either equilibrium or kinetic description in Eq. (5.5), assuming a Cassie-type relationship in the contact angles at equilibrium yields, respectively,

$$V_{eq} = \frac{\gamma_{lv}(1 - \cos \theta_{100,r})}{3\mu \int_a^b \frac{dx}{\zeta}} \cdot \frac{Kc}{1 + Kc} \quad (5.12)$$

$$V_r = \frac{\gamma_{lv}}{3\mu \int_a^b \frac{dx}{\zeta}} \cdot \left[ 1 - \exp\left(\frac{-k_r c L}{V_r}\right) \right] \quad (5.13)$$

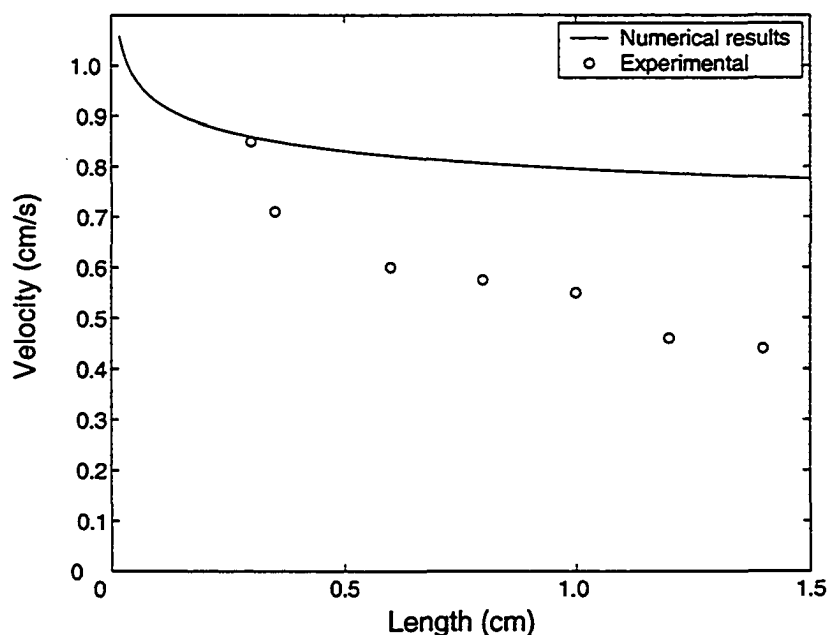


Figure 5.2: Numerical result without consideration of reaction mechanism;  $\circ$  represent data from Lee et al. [17].

where  $V_{eq}$  and  $V_r$  represent, namely, the velocities by equilibrium and kinetic description;  $\theta_{100,r}$  is the experimental contact angle when the adsorbate surface coverage is 100%;  $K$  and  $k_r$  are the adsorption constant and rate constant, respectively.

Figures 5.3 and 5.4 show the qualitative combination of the two reaction regimes. In both figures, the kinetic [expressed by Equation (5.13)], equilibrium [expressed by Equation (5.12)], and the hypothesized overall length/velocity relationship are represented by solid, dash, and bold lines, respectively. Specifically, Figure 5.3 was obtained with an assumed adsorption constant  $K$  of 550 L/mol and a rate constant  $k_r$  of 1000 L/(mol·s). Similarly, Figure 5.4 presents the case of the silane(decane)/glass system, with an assumed adsorption constant  $K$  of 700 L/mol, and a rate constant  $k_r$  of 1500 L/(mol·s). Stipulation of covalent, more

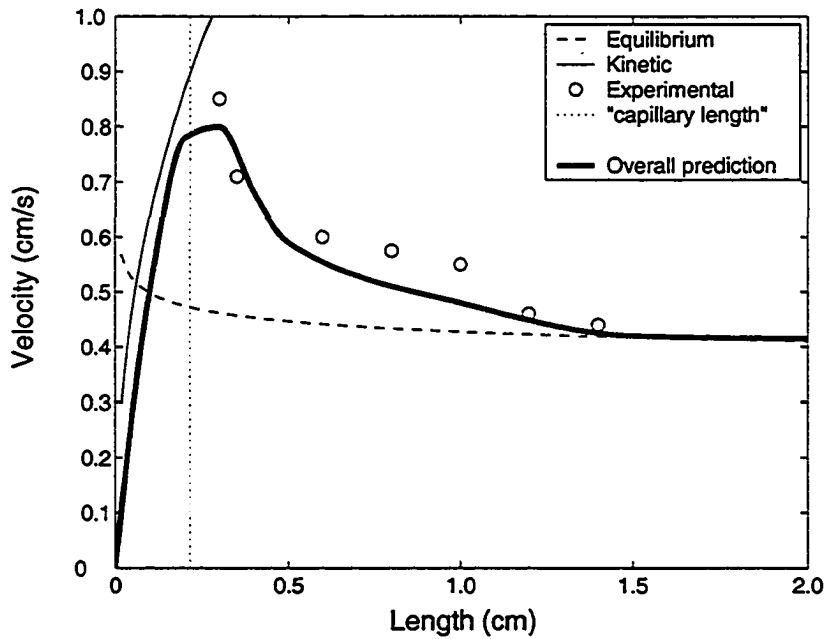


Figure 5.3: Overall length effect for the data from Lee et al. [17].

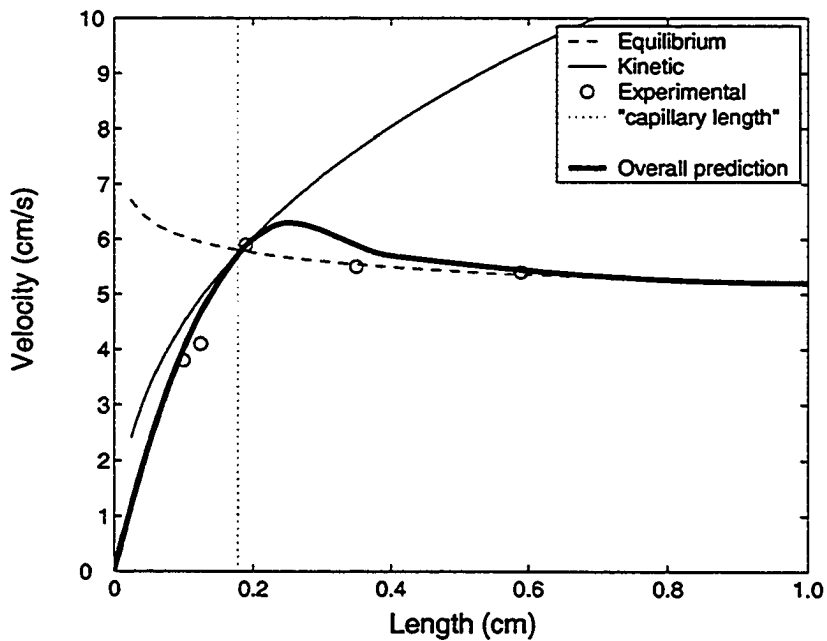


Figure 5.4: Overall length effect for data from Santos and Ondarçuhu [57].

robust silane adsorption [17] is supported by these parameters. The values of these constants, however, differ from those reported by Lee *et al.* and Dos Santos and Ondarçuhu. In order to construct the overall relationship for the two sets of experiments, the aim is not to obtain a general goodness of fit over all data points. For each adsorption system, there are parameters where the curves generated by Eqs. (5.12) and (5.13) bracket the experimental data, acting more-or-less like asymptotes. The Langmuir isotherm (Equilibrium) description is ideal for the case of an extremely long droplet, since the adsorption reaction is not restricted by the available sites. The reverse argument can be made about the kinetic assumptions, where the adsorption is treated as a rate process. At a given observed length, however, the experimental velocity response may be attributed (unevenly) to both idealized cases. By using the two idealized cases as asymptotes, the predicted overall relationship is essentially a weighted average of the contribution from both regimes.

There is a maximum possible droplet velocity for a given adsorption system (includes carrier liquid, adsorbate concentration, etc.). This maximum velocity and the gradual transition from kinetic to equilibrium regime is reflected in the results reported by Dos Santos and Ondarçuhu, as shown in Figure 5.4. From the reported data, the transition phase was overlooked by Dos Santos and Ondarçuhu [57], and was not observed by Lee *et al.* [17] In addition, Figure 5.5 shows the experimental results with a shorter amine species, dodecylamine, in the *n*-alkylamine(DHN)/thiol/gold system. Clearly, this results illustrate the existence of such a transitional phase. Note that the droplet lengths observed in the experiments of Lee *et al.* are large. By extension, a response similar to Fig. 5.5 should result if volume of the droplets are decreased. A prediction of overall relationship



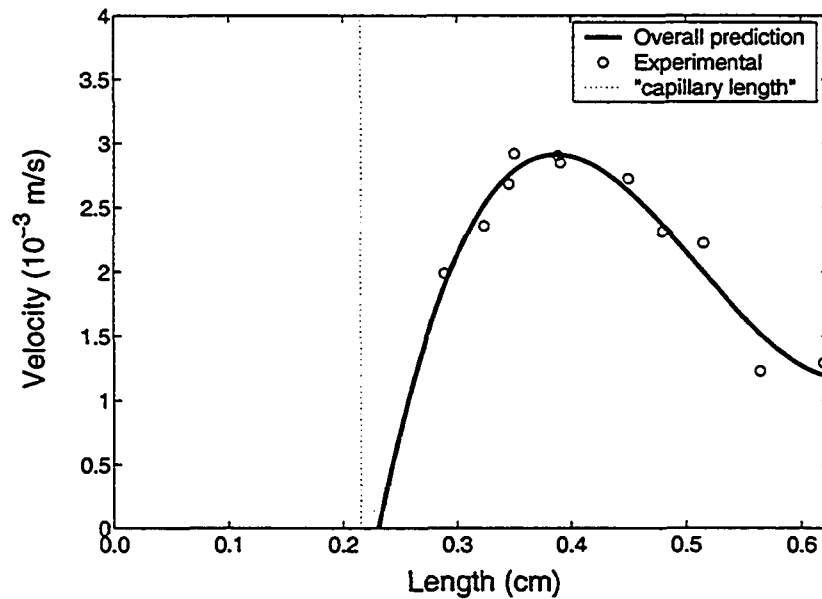


Figure 5.5: Observed length and velocity response for a dodecylamine(DHN)/thiol/gold system.

is shown in Figure 5.3.

The length of the droplet is a phenomenological quantity, such that its use in a mathematical argument effects engineering approximations at best. Therefore analogous equations such as Eqs. (5.12) and (5.13) are not offered for the overall relationship between observed droplet length and velocity. The overall responses in the respective figures were generated to guide the reader. These equations were derived to treat extreme cases of observed droplet lengths. A natural need thus arises for identifying these extreme cases quantitatively. The capillary length  $\lambda$  for DHN is 2.16 mm; for octane (used by Dos Santos and Ondarçuhu) it is approximately 1.78 mm. These values are marked on the respective figures by dotted vertical lines. It is noted that in both Fig. 5.3 and 5.4, the capillary length closely corresponds to the predicted maximum velocity for the given system. For Fig. 5.5, this correlation is less ideal. The capillary lengths have indication value

in these self-propulsion experiments. Phenomenologically, droplets with lengths greater than  $\lambda$  are better treated with equilibrium [Eq. (5.12)]; adsorption kinetics [Eq. (5.13)] is more suitable for droplets with lengths smaller than  $\lambda$ . Since the capillary length corresponds to an inflection from kinetic to equilibrium regime, it is also an indication of the maximum velocity that exists in its vicinity.

### 5.3 Summary

This chapter presented an analysis of the forces involved and examine whether kinetic or equilibrium approaches should be used for reactive wetting systems. It is found that the suitable treatment for droplet adsorption progress can be inferred from the relative length of the droplet. Increased adsorption reaction and the increased drag force associated with a longer droplet compete with each other, resulting in an overall length effect on droplet velocity. The experimental trend difference is quantified by combining the two ideal reaction regimes. The overall relationships between droplet length and velocity can be hypothesized. The existence of a transition zone in an overall length/velocity description is proposed. And the use of capillary length (of the carrier liquid) as a good indication to the adsorption reaction progress was supported by locations of maximum velocity in the predicted curves. An accurate description of the droplet profile such as the Laplace equation of capillarity must be employed for viscous-shear force. Perhaps the best description of the experimental result is: a droplet moving at  $v$  velocity appears to have an average separation between its front and wake. This suggest an evolutionary course — a simulation from which the length of a liquid droplet is a consequence of the velocities of the wetting edges. This is the step which was taken in the previous chapter.

## CHAPTER 6

### APPLICATION: SELF-BREAKUP OF DROPS

The concept of Lab-on-a-chip has led to many novel solutions against the practical problems of miniaturization. The main challenge in microfluidics has been to compensate for factors which are enhanced by shrinking a fluid system. In a typical microfluidic device, laminar flow is the dominant regime, and surface effects are significant due to the closeness of the bulk to interfacial regions. In many investigations, the eventual goal is to obtain a miniature fluidic device suitable for analysis of chemicals. For these applications, the continuous microchannel flow has the additional deficiency of sample dilution. To sustain the chemical kinetics, the analyte flow requires further concentration; this is in fact a non-trivial task [65]. Thus, it would benefit a miniature analytic system to retain sample concentration. Toward this end, one may utilize immiscible fluid plugs to transport the sample. Another alternative could be found in the use of discrete drops, which avoids many hurdles presented by miniaturization altogether. Nevertheless, separation of the already minute discrete drops on surfaces in a controlled manner is challenging. For example, a fundamental limit exists in contemporary drop-transport methods utilizing the electro-wetting phenomenon. These devices cannot produce nor transport a droplet of volume smaller than the size of the electrodes employed [66]. This chapter outlines a method to breakup discrete drops by

inducing three-phase contact line instability, causing them to self-divide as they move on chemically-patterned surfaces. The ability to divide and transport drops of very small volume directly on-chip without external means is demonstrated.

## 6.1 Methodology

It has been reported that motion in the three-phase contact line of a discrete liquid droplet can be induced by a solid surface energy gradient [17, 57–59]. These experiments were carried out under atmospheric conditions on smooth substrates. The drop translates in an unpredictable manner, reflecting the intrinsic nature of molecular adsorption modifications through formation of self-assembled monolayers (SAMs). The adsorption experiments are extended here by placing regions of hydrophobic restriction as 2-D barriers on the solid-vapor interface prior to an experiment. This hydrophobic region does not accept further surface modification and can direct the movement of liquid drops. By means of micro-contact printing, a branched 2D hydrophobic barrier ( $\approx 20 \text{ \AA}$  in height) is patterned onto the track and presented in front of a moving droplet. Figure 6.2 illustrates schematically a moving droplet traveling on the track at time  $t = 0$  (stage 1). As the hydrophobic barrier does not accept surface modification, the translating drop is forced to breakup by tearing the three-phase contact line apart at a location where the liquid-vapor and solid-vapor interfaces intersect forming a contact angle (stages 2 and 3). It is important to examine this three-phase contact line instability and how various 2D geometries affect the breakup of droplets on surfaces.

If the drop cannot be constrained, it will assume a dynamic equilibrium geometry until it comes into contact with the non-wetting boundary. Whether the geometry of a drop is highly curved depends on the volume and the surface ten-

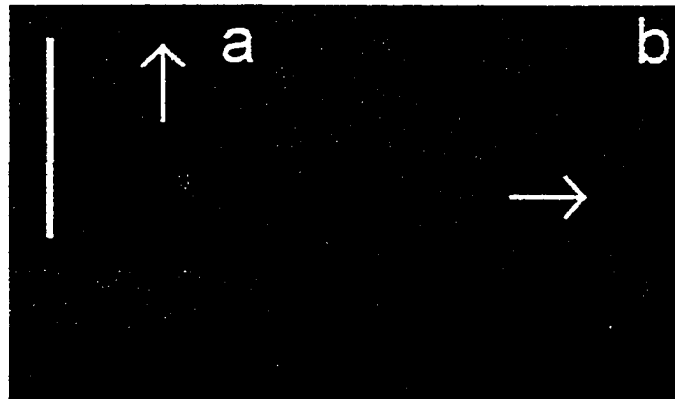


Figure 6.1: Captured image of: a) Top-view of the front and wake of a moving liquid volume under sufficient, rectangular wetting restriction; b) Macroscopic observation of the same liquid drop from the side; note that the reflection of the profile is also visible. The line in a) represents the length of 10 mm; b) is scaled differently. Note that the front geometry of a) is nearly symmetric about the center of the rectangular track.

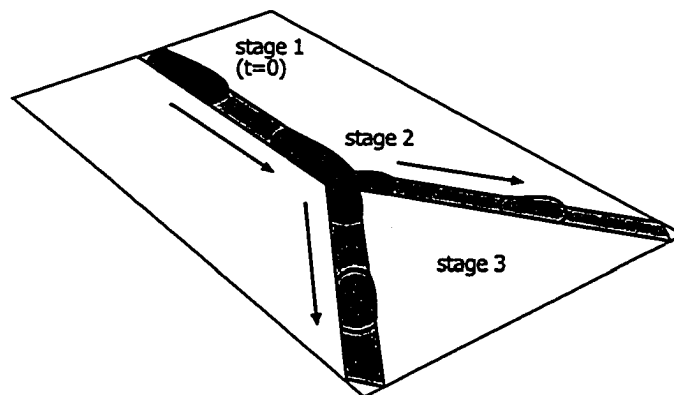


Figure 6.2: Schematics of the branching hydrophobic surface modification and its anticipated effect

sion  $\gamma_{lv}$  of the liquid drop. It is interesting to observe in Figure 6.1 that portion of the contact perimeter near leading front is an arc segment of almost constant geometry, while the bulk and its contact line (wake) may fluctuate. The shape of the front is to a first approximation symmetric about an axis parallel to the direction of the drop motion. Taking advantage of this symmetry, consider the branching of one path into a number of smaller veins, again via wetting restriction. The front is punctured as it encounters the hydrophobic surface area, and it conforms to the contour of the restriction much like water flow in pipes, see Figure 6.2. Equal volumes of the original drop are drained into the branches. The wake is eventually punctured by the non-wetting area, and the original volume is divided into a number of smaller droplets, each of approximately equal volume.

## 6.2 Results and discussion

The time sequence of drop breakup of a typical experiment is shown in Figure 6.3a). The initial track has a width of 1.5 mm, branching into two narrower veins of width 1.0 mm each. These dimensions were chosen to present a symmetric three-phase contact front. The initial drop volume was 1.5  $\mu\text{L}$ ; evaporation to the environment can be neglected at room temperature. The movement of liquid volume has been correctly anticipated. This specific drop exhibits a constant speed of 7.61 mm/s in an unbranched (1.5 mm wide) rectangular restriction. The speed of each deposited drop is phenomenologically related to its apparent length [61] and the concentration of surfactants. In general, longer drops exhibit slower speed. As predicted, the front deforms to the contour of a hydrophobic region and the wake separates cleanly. The two resulting droplets are approximately equal in volume; this can be inferred from the similar apparent lengths. Due to the difficulty in

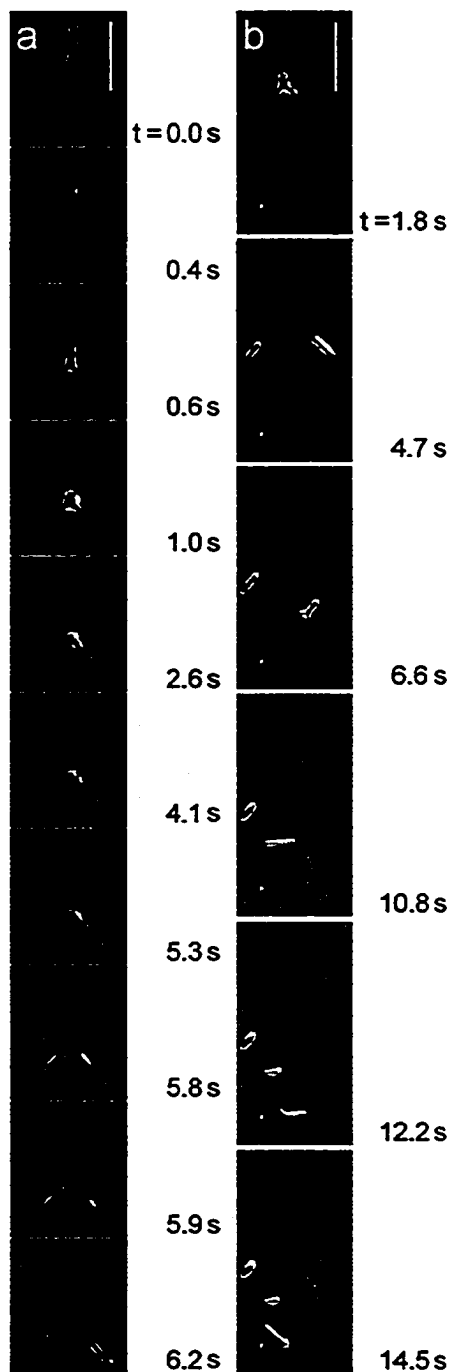


Figure 6.3: Captured sequential (top-to-bottom), top-view images of: a) The splitting of a liquid drop b) Performing three divisions on a single liquid volume. The restriction geometry is given to guide the eye. The dimension lines provided represent 10 mm; the quantity beside each image represent the time elapsed in seconds.

illuminating thin contact edges in the experimental setup, a closed contact line cannot always be observed in the images. Consecutive divisions which differ only in scale can also be performed. Fig. 6.3b) shows three such divisions, performed consecutively. Each of the latter junctions are smaller than its predecessor by  $2/3$ . The incomplete separation in the third junction (at  $t = 14.5$  s) is attributed to a lack of surface area that is required for adsorption. Clearly, the most important component of these systems is the geometry of the junction where the front is initially deformed. An asymmetry in front geometry could lead to a disproportionate drainage of the original drop into the veins. The next task is to design a number of different junction geometries to better understand the breakup of drops when in contact with a hydrophobic region.

Figure 6.4 illustrates the test geometries as drop separation devices, with their approximate performance. The quantities under each geometry indicate the separated drop volumes and the approximate reliability of the design for equal-volume division over the number of tests conducted. In each case, the initial volume was  $1.5 \mu\text{L}$  and six independent trials were made. Two significant issues regarding the wetting of the front may be observed. Figure 6.5a) illustrates drop breakup on non-wetting geometries with sharp, tip-like boundary much smaller than drop dimension. The separation of drop in this geometry does not perform as anticipated. In addition, the bulk of the drop displays a tardy motion through any branching in its path due to liquid surface tension. A continued translation of the front in spite of this tardy response effects a considerably thinned fluid over the entire perimeter. This is especially true when the liquid passes a hydrophobic region with some critically small width. In these cases, the contact line often collapses locally and satellite volumes are freed from the main drop. Whereas these satel-



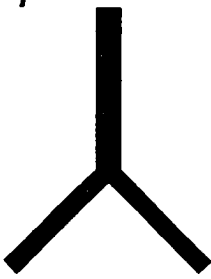
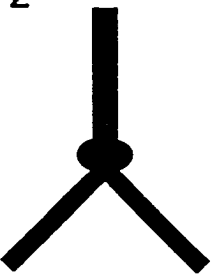
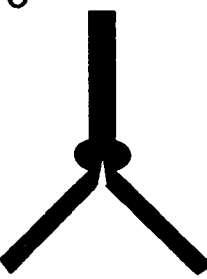
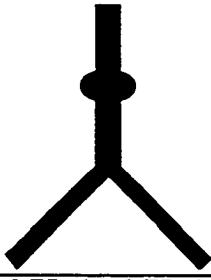
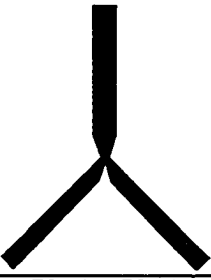
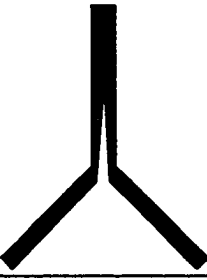
1	2	3
		
0.75 $\mu\text{L}$ - 0.75 $\mu\text{L}$	0.75 $\mu\text{L}$ - 0.75 $\mu\text{L}$	0.75 $\mu\text{L}$ - 0.75 $\mu\text{L}$
100 %	80 %	60 %
4	5	6
		
0.75 $\mu\text{L}$ - 0.75 $\mu\text{L}$	50 nL - 50 nL	unstable
100 %	100 %	0 %

Figure 6.4: Trial hydrophobic junction geometries and their respective performance

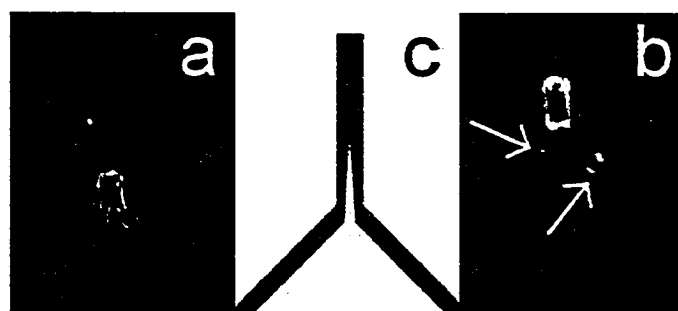


Figure 6.5: Captured top-view image of: a) A hydrophilic area being covered by the liquid volume due to surface tension. b) The *pinching* effect; the satellite volumes may be located at the point of the arrow. c) The junction design; shaded region represents a hydrophilic area. The restriction geometries are provided to guide the eye.

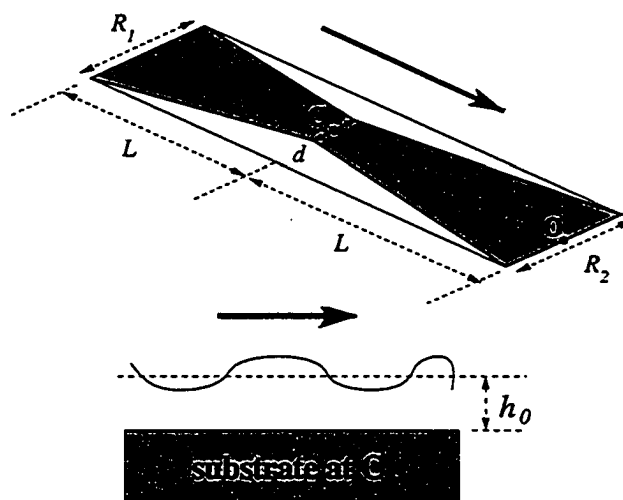


Figure 6.6: Diagrams of the geometry employed for analysis of narrow wetting passage; the shaded area allows monolayer formation. The drop translates in the direction of the thick arrows.

lite volumes may continue to move, the remaining volume is then stifled due to a lack of surface energy gradient, see Fig. 6.5b). It is immediate that one can tear off minute amount of an initial volume through this *pinchoff* action. Experiments have shown that a drop of approximately 50 nL or less can be obtained from an original 1.5  $\mu\text{L}$  with a single junction. The sequential operation of pinching and equal-division can lead to a very minute droplet volume. The precise control over this phenomenon has been difficult, hence the resulting tear droplet is often of arbitrarily small volume. If one wishes for an equal-division operations, this pinchoff must be understood.

The pinchoff action that frequently occurs in narrow constrictions is strictly related to circumstance of the drop, in particular the geometry of the junction akin to Figure 6.6. It is observed that the failing of any narrow hydrophobic junction is dictated by the occurrence of two events. Firstly, the drop must send a finger across point C and resume translation to gain fresh, unmodified surface. Second,

the interface must not be separated by necking and pinchoff. The shape of the interface of a finger is governed by the Laplace-Young relation describing pressure  $P$ :

$$\Delta P = \gamma_{lv}\kappa, \quad (6.1)$$

where  $\kappa$  is the mean curvature of the liquid vapor interface, and  $\gamma_{lv}$  is the liquid surface tension. Assuming frictionless, irrotational flow, the Bernoulli equation for the pressure difference is employed. Velocity  $u$  can be substituted with a scalar potential  $\phi = \nabla u$ , giving:

$$\frac{\partial \phi}{\partial t} + \frac{1}{2}|\nabla \phi|^2 + \frac{\kappa\gamma_{lv}}{\rho} = 0, \quad (6.2)$$

where  $\rho$  and  $u$  are respectively density of the liquid and the normal velocity of the interface. Evolutionary simulation on another form of the Eq. (6.2) has been performed and excellent insight had been gain regarding the motion of a liquid-vapor interface [8]. However, Eq. (6.2) will simply be employed to obtain the flow in the finger due to the deviation from a static Laplace-Young shape. A drop necessarily ceases translating when such a flow is equal to that caused by reactive-wetting. Manipulating Eq. (6.2) and using the definition of  $\phi$ :

$$Q = - \int \frac{\gamma_{lv}^t}{\rho} (\nabla \kappa) dA, \quad (6.3)$$

where  $Q$  is the volumetric flow rate across the interfacial area  $A$ , and  $t$  is a time scale on which the acceleration  $\partial \phi / \partial t$  acts. Eq.(6.3) predicts a large local velocity at the interface (to retract inward) if the local gradient of the mean curvature is large. This is an antagonistic flow which, when sufficiently large, can stall the moving finger of the drop.

The narrow junction design is also pronounced unstable if the finger of the

drop pinchoff after it passes point C. A narrow passage induces necking of the liquid drop, leading to an inviscid pinchoff similar to that which has been thoroughly investigated recently [67–69]. Experiments on a variety of narrow geometries similar to Fig. 6.6 were performed with varying values of  $R_2$  and  $d$  to scrutinize the stability of a narrow junction. For each junction design, six or more independent experiments were performed to collect statistics. The performance of passage is evaluated on a binary basis — whether a drop translates through the junction in entirety. A step-like relationship between the dimensions of the junction and its binary performance is expected, which represents a criticality of  $d$ . Approaching the critical  $d$  value from below, the average performance should be a percentage ( $<1$ ) reflecting the probability of successful transport. The relative geometry of the narrow junction can be described non-dimensionally by  $\mathcal{R} = (R_1 - d)/L$ , which represents the slope of the narrow passage in Fig. 6.6. Large  $\mathcal{R}$  represents narrow passage, and vice versa. Figure 6.7a) shows clearly that the experiments exhibit the step-like critical behavior at the relative ratio of  $\mathcal{R} = 0.45$ .

It is known that Lattice Boltzmann Method produce results that obey the Laplace Law, hence such a simulation is used to show finger retraction due to large Laplacian flow. The reactive-wetting experiments has been simulated in Chapter 4 using a D3Q19 Lattice Boltzmann Method. In this chapter the methodology of Kang *et al.* [70] is closely followed. The implementation has been examined for stability with respect to static conditions before simulation of reactive-wetting. By calculating in lattice units according to Eq. (6.3), it can be observed that a sharp increase in inward Laplacian flow always precedes the stalling of a simulated moving drop; see Figure 6.8. Also evident in these figures is the critical ratio  $\mathcal{R}$ . In simulation,  $\mathcal{R}$  is found to be 0.40; this value is comparable to the

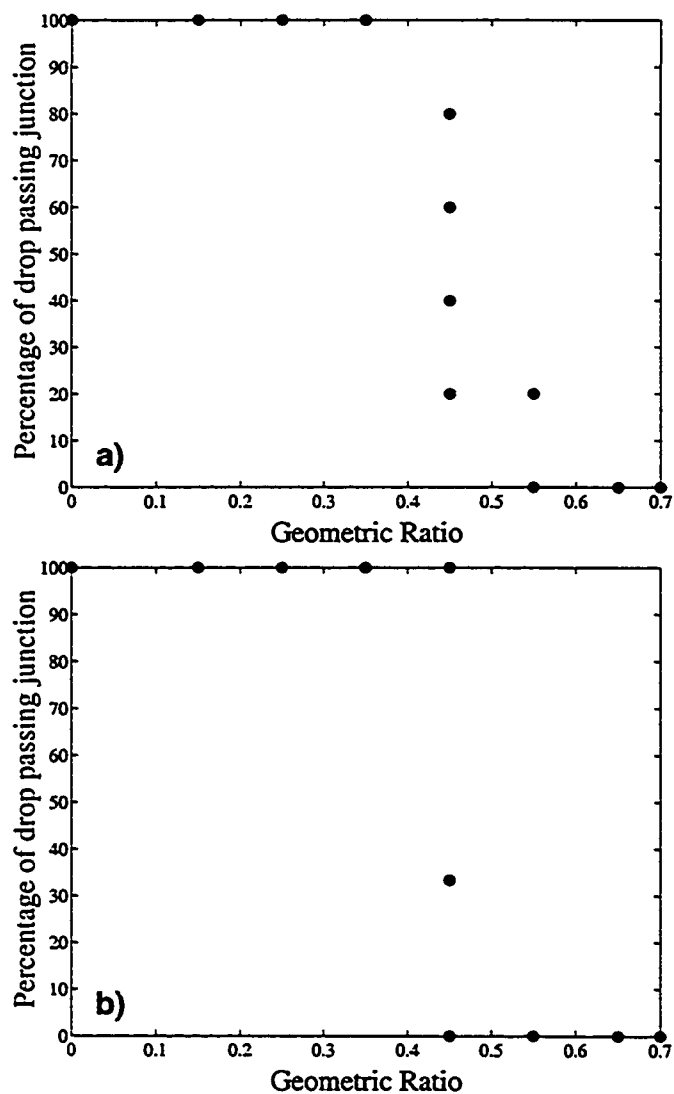


Figure 6.7: Average response of reactive-wetting drops on narrow junctions, characterized by ratio  $(R_1 - d)/L$  a) vibration-isolated b) under vibration

experimental result of 0.45. The discrepancy between the simulated and experimental critical values is attributed to the non-continuous sampling of  $d$ . The close comparison validates that the retraction of a reactive-wetting drop through narrow passages is indeed the result of surface flow caused by a Laplacian flow at the interface. The success of a lattice-gas simulation in a problem which has been traditionally treated with the lubrication approximation is an indication that a new analysis is required. It is also suspect that the wetting of liquids is not well-suited to a Navier-Stokes approach.

The stability of self-breakup devices against vibrations of the substrate is next demonstrated. For a gravity-bounded liquid drop, the collapse is possible due to unstable growth of a small, local perturbation. By applying a long-wave liquid film approach, this is shown not to be the case. The evolution equation of the liquid film height,  $h$ , is (*c.f.* Eq. (2.29) in [71])

$$\mu \partial_t h + \frac{\gamma_{lv}}{3} \partial_x (h^3 \partial_x^3 h) - \frac{\rho g}{3} \partial_x (h^3 \partial_x h) + \frac{A}{6\pi} \partial_x \left( \frac{h^3 \partial_x h}{(\alpha + h)^4} \right) = 0, \quad (6.4)$$

where  $\rho$  and  $\gamma_{lv}$  is the fluid density and surface tension, respectively;  $A$  is an infinite-finite-plate Hamaker constant between the solid surface and the liquid;  $g$  is assumed downward-negative. Equation (6.4) includes the effects of gravity, surface tension and long-range van der Waals (VDW) forces. Using a perturbation of  $h = h_0 + h'$  and upon linearization around the mean height  $h_0$ , Eq. (6.4) leads to the characteristic equation

$$S = h_0^2 \left[ \frac{A}{6\pi \gamma_{lv} (\alpha + h_0)^4} - \frac{1}{3} \frac{\rho g}{\gamma_{lv}} \right] K^2 - \frac{1}{3} K^4 \quad (6.5)$$

where  $S(=\mu s h_0 / \gamma_{lv})$  and  $K(=k h_0)$  are non-dimensional growth/decay and frequency ( $k/2\pi$ ) of the perturbation  $h'$ , respectively.

From Eq.(6.5) there exists a critical frequency range within which film collapse occurs if the coefficient to the quadratic term as written is positive. Monotonic behavior, where perturbation  $h'$  is stable over all frequencies, occurs if this coefficient is negative. The long-wave analysis illustrates that precaution against vibration was pertinent. However, if one assumes the frequency of long-wave film perturbation is equal to that of the substrate motion, then the system in employment is generally stable. When Eq. (6.5) is substituted with appropriate quantities, the quadratic coefficient is strictly positive down to a film height of approximately 10 nm, at which point a perturbation can effect instability in the film. Therefore, the growth of long wave perturbation does not affect the performance of the device unless the film height is below the above mentioned value. Fig. 6.7b) illustrates narrow-junction experiments conducted while the substrate is oscillated via a standardized vibration table at 10, 100, and 1000 Hz (respectively in the  $20\pi h_0$ ,  $200\pi h_0$ , and  $2000\pi h_0$  in non-dimensional  $K$ ). This further supports the prediction that vibration is negligible for the microfluidic device.

A limit on the number of these divisions exists obviously due to the atomicity of fluids — there can be no statistical behavior from an arbitrarily small number of molecules. The primary limiting factors include the evaporation at small drop volume and the molecular adsorption kinetics. Although evaporation can be successfully controlled, the management of the adsorption kinetics is difficult. Specifically, the molecular species in the carrier liquid is a consumable in the device. For design purpose, one needs to minimize the area which must be modified due to the limited solubility of these surfactants. As noted, the ratio of characteristic dimensions of a constrained liquid volume affect whether its contact perimeter experiences an instability and collapses. The wetting area must be small

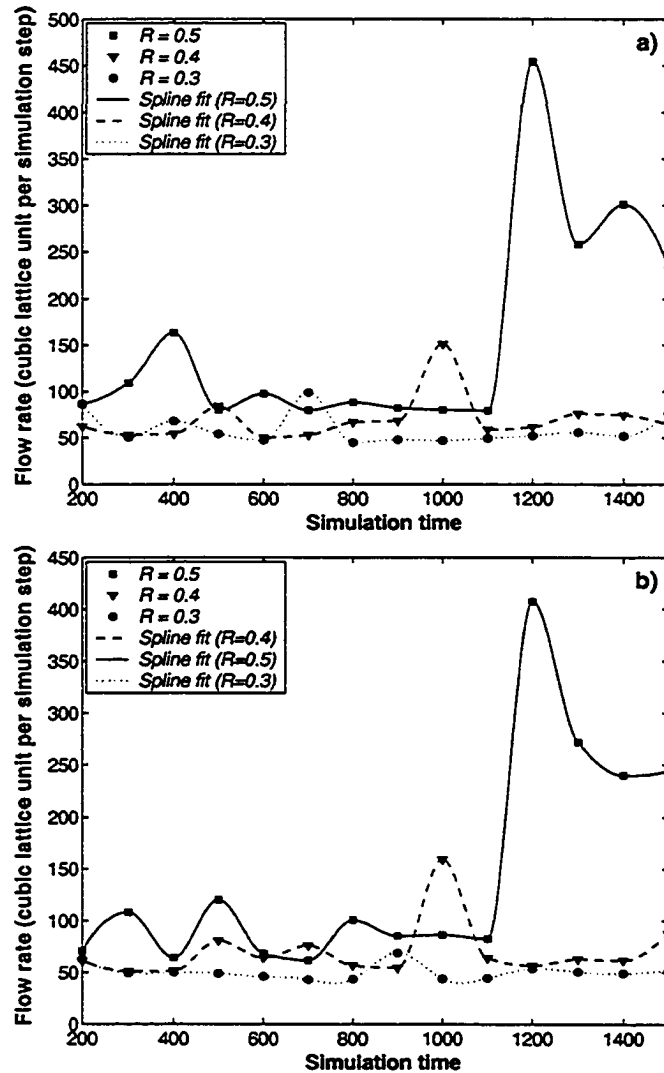


Figure 6.8: Laplacian flow inside narrow reactive-wetting drops through LBM simulation. The figures are simulations representing different rates of surfactant adsorption, which is adjusted through Eq. (4.1). Simulations in a) were performed with the parameter  $k = 0.001$ ; those in b) were performed with the parameter  $k = 0.01$ .



to conserve surfactants, but not critically small to cause pinching. In addition, the adsorption of the surfactant is concentration dependent. The effect of multiple divisions on the transport of these surfactants within a liquid volume has not been thoroughly studied. At low surfactant concentrations, it is reasonable that the adsorption may not provide a significant surface energy gradient, or the free energy is such that no adsorption from solution can occur. This latter scenario has been observed in experiments with similar close-packed, mono-molecular films [24]. In general, the specifications of a transport/break-up system must be particular to its goals; at the present an all-purpose device is not practical.

The use of discrete liquid volume has obvious advantages over microchannel-type flow. The reported technique can serve as a tool for microfluidic chemical transport. The geometry of the hydrophobic areas requires optimization given a volume of liquid to be manipulated. Tear droplets can be formed to have minute volume; equal division of a volume is easily achieved. The sequential implementation of these two procedures is also possible. While there are many other controlled methods which effect small volumes, this system is the only one which requires no external input. It is immediately applicable in the transport and division of colloidal parcels within a carrier liquid on portable, Lab-on-a-chip systems.

### 6.3 Summary

This chapter presented a method to successfully separate discrete droplets on surfaces, without external input, through induced three-phase line instability. By branching of hydrophobic restriction, liquid drop can be forced to separate while translating on surface. Automation of this drop division process has been shown to depend on surface pattern geometry and three-phase line instability. Results have

shown that at least 3 near equal subdivision of a 1.5  $\mu\text{L}$  drops can occur. Smaller satellite drops can also be obtained through induced contact line instability.

## CHAPTER 7

### CONCLUSIONS AND FUTURE WORK

#### 7.1 Summary

The investigation and subsequent application of the Reactive-Wetting phenomenon has been presented in this thesis. The thesis addresses the phenomenon via both experimental and computational methods. It was shown that phenomenological length of a constrained moving drop can be related to its translating velocity. A transition of adsorption scheme is found to exist. Hence an optimal length for drops constrained by rectangular hydrophobic patches is attained during the apex of the transition from kinetic to first-order Langmuir adsorption. Although gravity has adverse effects on the Reactive-Wetting drops, it can be rendered negligible by reducing the droplet volume. Surface-ascending drops are found to have decreased velocity with increased substrate acclivity. The drop profile of an ascending drop can be significantly asymmetric to effect a change in contact area, hence velocity. Hydrophobic restrictions can act like piping to force separation, necking, and pinchoff of moving drops. A practical device for microfluidic transport has been developed based on this concept and its performance has been evaluated. Low amplitude vibration of the device at low or high frequencies has little effect on the performance of rectangular or narrow junctions. The device can produce

approximately binary divisions of a given drop volume consecutively, for at least a maximum of 7 divisions. With proper consideration of the critical geometric ratio for a narrow junction, the device can predictively pinchoff a minute droplet having a minute portion of the original volume. The motion of a drop at a narrow junction is reasoned to have two stages. Only the latter stage can lead to pinchoff.

D3Q19 Lattice-Boltzmann simulations led to the conclusions that the quasi-dynamics of the moving droplet can be well-predicted by computational methods. A cell size of  $50(X)$  by  $20(Y)$  by  $20(Z)$  was capable of producing velocity trend for surface-ascending drops similar to that produced by experiment. The simulations performed in a lattice cell of size  $50(X)$  by  $50(Y)$  by  $20(Z)$  replicated the experimental geometric ratio in pinchoff cases by producing the first stage of motion. However, in the present implementation, Lattice-Boltzmann methods cannot reproduce the pinchoff of minute droplets via the second, kinetically-inclined stage.

## 7.2 Future direction

There are several interesting aspects of the Discrete-Reactive-Wetting experiment that warrant future investigation:

1. The transfer of surface chemical energy gradient is expressed mechanically here in a DRW experiment. The use of DRW to drive mechanical motion other than the liquid can be useful in engineering. Through a cursory experiment, I have already shown that pushing of immiscible drops is possible. Future use of surface chemical gradient can lead to other types of energy transfer.

2. The emphasis on analytic methods can lead to other descriptions of the phenomenon that aid in understanding. Specifically, statistical mechanical models similar to that used for phase-transition can be employed. The successful use of Lattice-Boltzmann Method in simulating the moving drops suggest that such an approach should be taken.
3. The present implementation of the Lattice Boltzmann Method responds aphysically to large forces, thus making it incapable of simulating kinetically-inclined systems where the forces involved locally large. Improvement on the method can yield a computational scheme which simulate both stages of the pinchoff phenomenon.

## BIBLIOGRAPHY

- [1] A. Ulman, *Chem. Rev.* **96**, 1533 (1996).
- [2] F. Brochard, *Langmuir* **5**, 432 (1989).
- [3] P. G. de Gennes, *Reviews of Modern Physics* **57**, 827 (1985).
- [4] R. J. Braun, B. T. Murray, W. J. Boettinger, and G. B. McFadden, *Physics of Fluids* **7**, 1797 (1995).
- [5] J. B. Freund, *Physics of Fluids* **15**, L33 (2003).
- [6] D. Ausseré, A. M. Picard, and L. Legér, *Physical Review Letters* **57**, 2671 (1986).
- [7] L. Legér, M. Erman, A. M. Guinet-Picard, D. Ausseré, and C. Strazielle, *Physical Review Letters* **60**, 2360 (1988).
- [8] D. Leppinen and J. R. Lister, *Physics of Fluids* **15**, 568 (2003).
- [9] D. Y. Kwok and A. W. Neumann, *Advances in Colloid and Interface Science* **81**, 167 (1999).
- [10] A. Ulman, *An Introduction to Ultrathin Organic Films* (Academic Press, Boston, 1991).
- [11] F. Schreiber, *Prog. Surf. Sci.* **65**, 151 (2002).

- [12] H. Fenniri, P. Mathivanan, K. L. Vidale, D. M. Sherman, K. Hallenga, K. V. Wood, and J. G. Stowell, *J. Am. Chem. Soc.* **123**, 3854 (2001).
- [13] H. Fenniri, B.-L. Deng, A. E. Ribbe, K. Hallenga, J. Jacob, and P. Thiagarajan, *Proc. Natl. Acad. Sci. USA* **99**, 6487 (2002).
- [14] S. Vauthey, S. Santoso, H. Gong, N. Watson, and S. Zhang, *Proc. Natl. Acad. Sci. USA* **99**, 5355 (2002).
- [15] M. F. Perutz, B. J. Pope, D. Owen, E. E. Wanker, and E. Scherzinger, *Proc. Natl. Acad. Sci. USA* **99**, 5596 (2002).
- [16] M. Mrksich and G. M. Whitesides, *Ann. Rev. Biophys. Biomol. Struct.* **25**, 55 (1996).
- [17] S.-W. Lee, D. Y. Kwok, and P. E. Laibinis, *Phys. Rev. E* **65**, 051602 (2002).
- [18] P. Silberzan, L. Leger, D. Ausserre, and J. J. Benattar, *Langmuir* **7**, 1647 (1991).
- [19] G. E. Poirier and E. D. Pylant, *Science* **272**, 1145 (1996).
- [20] O. Dannenberger, M. Buck, and M. Grunze, *J. Phys. Chem. B* **103**, 2202 (1999).
- [21] K. A. Peterlinz and R. Georgiadis, *Langmuir* **12**, 4731 (1996).
- [22] G. E. Poirier, M. J. Tarlov, and H. E. Rushmeier, *Langmuir* **10**, 3383 (1994).
- [23] F. Schreiber, A. Eberhardt, T. Y. B. Leung, P. Schwartz, S. M. Wetterer, D. J. Lavrich, L. Berman, P. Fenter, P. Eisenberger, and G. Scoles, *Phys. Rev. B* **57**, 12476 (1998).

- [24] W. C. Bigelow, D. L. Pickett, and W. A. Zisman, *J. Colloid Sci.* **1**, 513 (1946).
- [25] M. Brust, M. Walker, D. Bethell, D. J. Schiffrin, and R. Whyman, *J. Am. Chem. Soc. Commun.* p. 801 (1994).
- [26] R. C. Thomas, L. Sun, and M. Crooks, *Langmuir* **7**, 620 (1991).
- [27] O. Chailapakul, L. Sun, C. Xu, and M. Crooks, *J. Am. Chem. Soc.* **115**, 12459 (1993).
- [28] A. Ulman and N. Tillman, *Langmuir* **5**, 1418 (1989).
- [29] L. Sun, R. C. Thomas, R. M. Crooks, and A. J. Ricco, *J. Am. Chem. Soc.* **113**, 8550 (1991).
- [30] M. L. Schilling, H. E. Katz, S. M. Stein, S. F. Shane, W. L. Wilson, S. Buratto, S. B. Ungahse, G. N. Taylor, T. M. Putvinski, and C. E. D. Chidsey, *Langmuir* **9**, 2156 (1993).
- [31] L. Bertilsson and B. Liedberg, *Langmuir* **9**, 141 (1993).
- [32] H. Keller, W. Schrepp, and H. Fuchs, *Thin Solid Films* **210/211**, 799 (1992).
- [33] R. G. Nuzzo and D. L. Allara, *J. Am. Chem. Soc.* **150**, 4481 (1983).
- [34] E. Ostuni, L. Yan, and G. M. Whitesides, *Colloids Surfaces B* **15**, 3 (1999).
- [35] Y. Nishikata, M. aki Kakimoto, A. Morikawa, and Y. Imai, *Thin Solid Films* **160**, 15 (1988).
- [36] B. Bhushan, *Modern Tribology Handbook* (CRC Press LLC, 2001).



- [37] S. R. Wasserman, G. M. Whitesides, I. M. Tidswell, B. M. Ocko, P. S. Pershan, and J. D. Axe, *J. Am. Chem. Soc.* **111**, 5852 (1989).
- [38] R. G. Nuzzo, L. H. Dubois, and D. L. Allara, *J. Am. Chem. Soc.* **112**, 558 (1990).
- [39] L. S. Jung and C. T. Campbell, *J. Phys. Chem.* **104**, 11168 (2000).
- [40] G. E. Poirier, *Chem. Rev.* **97**, 1117 (1997).
- [41] T. Ishida, S. Tsuneda, N. N. M. Hara, H. Sasabe, and W. Knoll, *Langmuir* **13**, 4638 (1997).
- [42] M. Kawasaki, T. Sato, T. Tanaka, and K. Takao, *Langmuir* **16**, 1719 (2000).
- [43] I. Doudevski, W. A. Hayes, and D. K. Schwartz, *Phys. Rev. Lett.* **81**, 4927 (1998).
- [44] J. Hautman and M. L. Klein, *J. Chem. Phys.* **91**, 4994 (1989).
- [45] P. Fenter, A. Eberhardt, K. S. Liang, and P. Eisenberger, *J. Chem. Phys.* **106**, 1600 (1997).
- [46] A. N. Parikh, D. L. Allara, I. B. Azouz, and F. Rondelez, *J. Phys. Chem.* **98**, 7577 (1994).
- [47] G. J. Kluth, M. M. Sung, and R. Maboudian, *Langmuir* **13**, 3775 (1997).
- [48] M. M. Walczak, D. D. Popenoe, R. S. Deinhammer, B. D. Lamp, C. Chung, and M. D. Porter, *Langmuir* **7**, 2687 (1991).
- [49] M. J. Han and D. Y. Kwok (2002), unpublished.

- [50] W. A. Zisman, *Friction, durability and wettability properties of monomolecular films on solids; Chapter (p.110-148) in Friction and Wear, Davies, R.* (Elsevier, Amsterdam, 1959).
- [51] S.-W. Lee, Ph.D. thesis, Massachusetts Institute of Technology (1999).
- [52] E. F. Hare, E. G. Shafrin, and W. A. Zisman, *J. Phys. Chem.* **58**, 236 (1954).
- [53] Y. Xia and G. M. Whitesides, *Angew. Chem. Int. Ed.* **37**, 550 (1998).
- [54] F. Laermer and A. Schlip (1994).
- [55] S. Lahooti, O. del Río, P. Cheng, and A. Neumann, *Applied Surface Thermodynamics* (Marcel Dekker Inc, New York, 1996).
- [56] D. A. Wolf-Gladrow, *Lattice gas cellular automaton and Lattice Boltzmann models: an introduction*, Lecture notes in mathematics (Springer, 2000).
- [57] F. D. D. Santos and T. Ondarçuhu, *Phys. Rev. Lett.* **75**, 2972 (1995).
- [58] M. K. Chaudhury and G. M. Whitesides, *Nature (London)* **256**, 1539 (1992).
- [59] K. Ichimura, S.-K. Oh, and M. Nakagawa, *Science* **288**, 1624 (2000).
- [60] G. C. Mo and D. Y. Kwok, *J. Micromech. Microeng.* (2004), submitted.
- [61] G. C. H. Mo and D. Y. Kwok, *Colloids Surfaces A* **232**, 169 (2004).
- [62] F. M. White, *Fluid Mechanics* (WCB McGraw-Hill, 1999), 4th ed.
- [63] F. Brochard-Wyart and P. G. de Gennes, *C. R. Acad. Sci. Paris*, t. 321, Série IIb p. 285 (1995).

- [64] S. Hartland and R. W. Hartley, *Axisymmetric fluid-liquid interfaces* (Elsevier, 1976).
- [65] B. Zhao, J. S. Moore, and D. J. Beebe, *Science* **291**, 1023 (2001).
- [66] M. G. Pollack, R. B. Fair, and A. D. Shenderov, *Appl. Phys. Lett.* **77**, 1725 (2000).
- [67] R. F. Day, E. J. Hinch, and J. R. Lister, *Physical Review Letters* **80**, 704 (1998).
- [68] A. U. Chen, P. K. Notz, and O. A. Basaran, *Physical Review Letters* **88**, 174501 (2002).
- [69] J. C. Burton, J. E. Rutledge, and P. Taborek, *Physical Review Letters* **92**, 244505 (2004).
- [70] Q. Kang, D. Zhang, and S. Chen, *Phys. Fluids* **14**, 3203 (2002).
- [71] A. Oron, S. H. Davis, and S. G. Bankoff, *Rev. Mod. Phys.* **69**, 931 (1997).